



HAL
open science

Reconstruction of the Lagrangian deformation of the aorta from 4D MRI data

Mocia Agbalessi, Alain Lalande, Olivier Bouchot, Toshiyuki Hayase, Jean-Joseph Christophe, Miguel Angel Fernández, Damiano Lombardi

► **To cite this version:**

Mocia Agbalessi, Alain Lalande, Olivier Bouchot, Toshiyuki Hayase, Jean-Joseph Christophe, et al.. Reconstruction of the Lagrangian deformation of the aorta from 4D MRI data. 2021. hal-03349442v1

HAL Id: hal-03349442

<https://inria.hal.science/hal-03349442v1>

Preprint submitted on 20 Sep 2021 (v1), last revised 5 Sep 2023 (v3)

HAL is a multi-disciplinary open access archive for the deposit and dissemination of scientific research documents, whether they are published or not. The documents may come from teaching and research institutions in France or abroad, or from public or private research centers.

L'archive ouverte pluridisciplinaire **HAL**, est destinée au dépôt et à la diffusion de documents scientifiques de niveau recherche, publiés ou non, émanant des établissements d'enseignement et de recherche français ou étrangers, des laboratoires publics ou privés.

ARTICLE TYPE

Reconstruction of the Lagrangian deformation of the aorta from 4D MRI data

Mocia Agbalessi^{1,2,6} | Alain Lalande^{3,4} | Olivier Bouchot^{3,5} | Toshiyuki Hayase⁶ | Jean-Joseph Christophe⁷ | Miguel Angel Fernández^{1,2} | Damiano Lombardi^{1,2}

¹Sorbonne Université & CNRS, UMR 7598
LJLL, Paris, France

²Inria, Paris, France

³ImVia Laboratory, University of Burgundy,
Dijon, France,

⁴Department of Magnetic Resonance
Imagery, Dijon University Hospital, Dijon,
France

⁵Department of Cardio-vascular and
Thoracic Surgery, Dijon University
Hospital, Dijon, France

⁶CASIS - CArdiac Simulation & Imaging
Software, Quetigny, France

⁷Institute of Fluid Science, Tohoku
University, Sendai, Japan

Summary

This paper presents a novel approach to track objects from 4D Flow MRI data. A salient feature of the proposed method is that it fully exploits the geometrical and dynamical nature of the information provided by this imaging modality. The underlying idea consists in formulating the tracking problem as a data assimilation problem, in which both position and velocity observations are extracted from the 4D Flow MRI data series. Optimal state estimation is then performed in a sequential fashion via Kalman filtering. The capabilities of the method are extensively assessed in a numerical study involving synthetic and clinical data.

KEYWORDS:

4D flow MRI, data assimilation, Kalman filter.

1 | INTRODUCTION

Among cardiovascular diseases, arterial aneurysms (i.e., abnormal enlargement of arteries), depict a high risk of mortality^{1,2}. The natural evolution of this pathology is a more or less rapid growth of the dilatation that can lead to dissection or rupture of the arterial wall. These complications are extremely serious because of the high lethal risk. To prevent complications, surgery is proposed in current clinical practice, consisting in the removal of the aneurysm and the replacement of that aortic section by a synthetic tube in Dacron. The surgical decision follows guidelines^{3,4,5} which are solely based on the diameter of the aneurysm. The American Society of Vascular Surgery³ recommends for instance operative repair for patients with an abdominal aortic aneurysm larger than $50mm$. The European guidelines for intervention, provided by the the European Heart Journal⁴, are less restrictive with a threshold of $55mm$. The threshold can be lower, whether the patient presents additional risk or vascular syndromes ($50mm$ for patients with Marfan syndrome, $45mm$ for those with family history of cardiovascular disorders).

Recent studies⁶ showed that dissection and rupture can appear even when the aortic diameter is lower than $55mm$, in case of ascending aorta aneurysms and for patients without medical history. Consequently, there is a strong clinical demand for more robust predictive parameters of aortic aneurysm risk. Biomarkers derived from well-known parameters such as wall stiffness, wall shear stress (WSS), inlet flow jet angle, etc. are being increasingly investigated to assess the risk of rupture of aneurysm. In *Hope et al.*⁷, a correlation has been established between high growth rate of aortic aneurysm and abnormal flow displacement for the BAV (bicuspid aortic valve) patients.

The most convenient way to obtain those parameters is based on Phase Contrast Magnetic Resonance Imaging (PC-MRI)⁸, a medical imaging modality developed in recent decades with the aim of visualizing and quantifying the blood flow in the vasculature. In the literature, this imaging technique is also called 4D PC-MRI or 4D Flow MRI, because it includes time-resolved slice images covering a volume of acquisition, with flow encoding. It provides both anatomical (magnitude images) and

functional (phase images) information that enables the non invasive analysis of blood vessel hemodynamics, and consequently the assessment of flow driven parameters of interest. *Hope et. al*⁷ demonstrate a good reproducibility of the biomarkers computed through 4D Flow MRI. However, 4D Flow analysis requires extensive pre-processing. In particular, the extraction of the aortic geometry at each time step of the cardiac cycle may be needed. The manual contouring of the aortic lumen takes 20-30 minutes for each time step¹ and cannot be considered as viable part in any clinical routine. It is thus necessary to develop automatic segmentation algorithms of the aortic wall.

Note that the segmentation is to be distinguished from the reconstruction. The first aims at enhancing in the images (for example with a binary mask or contours) pixels belonging to an organ of interest (aorta), whereas with the latter, the geometrical configurations of this organ are extracted. For 4D Flow visualization and quantification, having a 3D geometrical configuration is required. The common practice is to extract one 3D patient specific aortic reconstruction, based (or not) on segmentation, and all biomarkers are calculated based on this configuration. However, more advanced parameters such as WSS are computed through numerical simulation, due to the limited space and time resolution of 4D MRI. WSS related biomarkers are increasingly investigated first to quantify the effect of abnormal flows, and then to localize risks of aneurysm and rupture. The first step to evaluate WSS is to identify the wall vessel. The reconstruction is usually done from Magnetic Resonance Angiographic sequences and results in a static geometry of the aorta. However, since the compliant aorta undergoes high vascular blood pressure, its deformation during the cardiac cycle is not negligible, and considering a single geometry to compute time-averaged biomarkers can yield significant error. *Perinajova et al.*⁹ studied the effect of the variability of the segmentation on the variability of the WSS distribution, with 4D MRI and CFD. This variability of segmentation tackled in the paper is by far negligible compared to the variability due to the time deformation of the aorta during the cardiac cycle. Consequently accurate WSS computation during the cardiac cycle should be done with time-dependent configurations. Robust and accurate techniques have been proposed for the time coherent segmentation of 4D MRI image sequences (anatomic series) of the aorta¹⁰, with minimal human intervention. The surface of the aorta can be afterwards reconstructed from 4D segmentation resulting in a series of mesh representing time configurations. It is not required for those meshes to have point-to-point correspondence. Notable work achieved the reconstruction of time configurations with point-to-point match, specifically for the left ventricle. In *Lim et al.*¹¹, 4D reconstruction of the left ventricle is performed with point-to-point correspondance. 2D contours lines are pre-segmented from time series of grayscale 3D images prior to applying the reconstruction. A patient specific template is reconstructed and deformed to fit the segmented contours, using a tree-based structure. Vertex-to-vertex match is calculated based on geometrical assumptions. Note that the twist of the ventricle is not captured. Using 4D Tagged MRI, the local deformation of the left ventricle endocardium can be better integrated in the reconstruction in terms of material point tracking¹². Tagged MRI is however limited to organs with sufficient thickness, meaning that assessing the local deformation of the aortic wall from Tagged MRI would be delicate.

The objective of this work is to propose a framework for object tracking from 4D Flow MRI using both geometrical and dynamical information. To the best of our knowledge, no velocity field (as a kinematical quantity) is actually integrated in the above mentioned studies. In particular, we propose a Kalman filter based method to reconstruct and track the aorta at every step of the cardiac cycle. The state is composed of both the position and the velocity of the mesh points. To this end, we also introduce an appropriate position observation operator that translates the grayscale images into a Lagrangian information.

The position observation operator that we propose extracts an aortic configuration based on the images. It mimics active contours approaches, based on the minimization of the sum of an internal and an external energy. The internal energy is an energy of deformation to ensure surface regularity. The external energy is often build from the gradient of image intensity. This way of balancing attraction to image high gradient areas and a regularity constraint is the spine of active contours methods^{13,14}. In fact, the image intensity gradient plays the role of a local external attractive force for a prior deformable model of the object. An internal force is formulated so as to control the elasticity and the resistance to large deformations. Active contours are often referred in the literature as "snake" algorithm. In the seminal paper of *Kass et al.*¹³, the active contours algorithm is initialized with a parametric spline, and the internal force is formulated with first order and second order derivative of the spline, expressed in parametric coordinates. Since the gradient can be noisy or have some irregularities, methods have been derived with a smoothed image gradient as in *Xu et al.*¹⁵. The external energy is expressed with a generalized gradient vector flow, which presents more regularity than the image gradient.

In the literature, active contours have been combined with Kalman filtering in order to achieve robust edge detection and has been applied for 3D CTA segmentation as in *Lee et al.*¹⁶ for instance, by tracking 2D contours from one slice to the other. Kalman

¹There is no standard time, but it depends on the expert.

filter has also been combined with active contours to perform 4D reconstruction of vessels from ultrasound¹⁷, by tracking the centerline of the vessel at specific time steps. An active contour algorithm is then introduced to reconstruct the vessels from the centerline. The reconstructed geometries are not necessarily related in terms of deformation assessment. A combination with optical flow adds relevant dynamical information, but its efficiency is limited to images with time-independent image intensity, and homogeneous image region. 4DMRI does not intrinsically fill those requirements. The position observation operator that will be introduced herein shares some similarities with active contour methods.

Kalman filter is applied to estimate the Lagrangian deformations from time-resolved images and velocity as provided by 4D flow MRI. Several other algorithms tackle the time reconstruction of moving parts of the heart from time-resolved image sequences^{18 12 11} using other approaches. They rely on pre-processed or pre-segmented images, and do not dispose of the richness of the flow information (eulerian velocity field), as available in 4D MRI. The mesh point tracking, when ensured, is performed through morphological hypotheses, image intensity or velocity approximations from complementary images with enhanced temporal resolution. Kalman filter offers a reasonable alternative to enrich image-based reconstruction from 4DMRI magnitude series with flow measurements, to tackle in a very natural way mesh point tracking. The geometrical observation operator is computed progressively and does not require image pre-processing, or pre-segmented images, even if it could benefit from the latter.

The rest of this paper is organized as follows. In the next section, the tracking problem is presented in both the continuous and the discrete settings. The position observation operator is presented in Section 2.3.1. After a brief presentation of Kalman filter, the proposed tracking algorithm is detailed in Section 3.2. Section 4 provides an extensive numerical assessment of this algorithm, involving synthetic and clinical data. Finally, a summary of the results and some conclusion with perspectives are drawn in Section 5.

2 | CONTINUOUS PROBLEM AND DISCRETIZATION

For a given final time instant $T > 0$, let $\boldsymbol{\phi} : \Gamma_R \times [0, T] \rightarrow \mathbb{R}^d$ describe the motion of a surface $\Gamma(t) := \boldsymbol{\phi}(\Gamma_R, t) \subset \Omega$, where $\Omega \subset \mathbb{R}^d$ denotes a fixed domain and Γ_R stands for the reference configuration of the surface $\Gamma(t)$. This surface evolves in Ω through the transport of the Eulerian velocity field $\mathbf{u} : \Omega \times [0, T] \rightarrow \mathbb{R}^d$, according to the following dynamics:

$$\begin{cases} \partial_t \boldsymbol{\phi}(\boldsymbol{\xi}, t) = \mathbf{u}(\boldsymbol{\phi}(\boldsymbol{\xi}, t), t), & (\boldsymbol{\xi}, t) \in \Gamma_R \times]0, T], \\ \boldsymbol{\phi}(\boldsymbol{\xi}, 0) = \boldsymbol{\phi}_0(\boldsymbol{\xi}), & \boldsymbol{\xi} \in \Gamma_R, \end{cases} \quad (1)$$

where $\boldsymbol{\phi}_0 : \Gamma_R \rightarrow \mathbb{R}^d$ stands for initial configuration of the surface (see Figure 1).

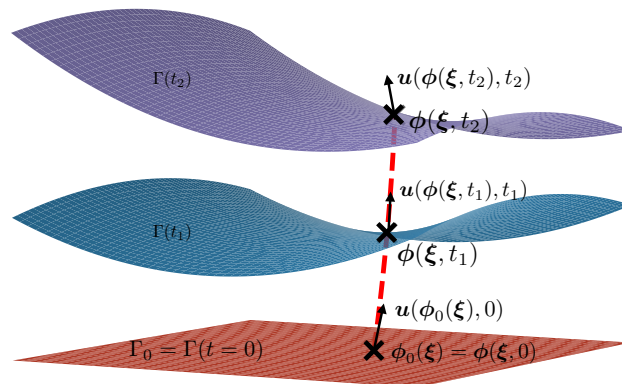


FIGURE 1 Illustration of the transport of $\Gamma(t)$ through the velocity field \mathbf{u} .

The problem considered in this paper consists in estimating the motion ϕ from the following information (see Figure 2):

1. geometric data: a grayscale image sequence described in terms of the scalar function $F_M : \Omega \times [0, T] \rightarrow \mathbb{R}$;
2. kinematic data: a measurement $\mathbf{u}_M : \Omega \times [0, T] \rightarrow \mathbb{R}^d$ of the Eulerian velocity field \mathbf{u} in Ω ;
3. an *a priori* information $\tilde{\phi} : \Gamma_R \times [0, T] \rightarrow \mathbb{R}^d$ on the unknown mapping ϕ .

The first two points correspond to the data traditionally provided by 4D flow MRI image sequences^{19,20}.

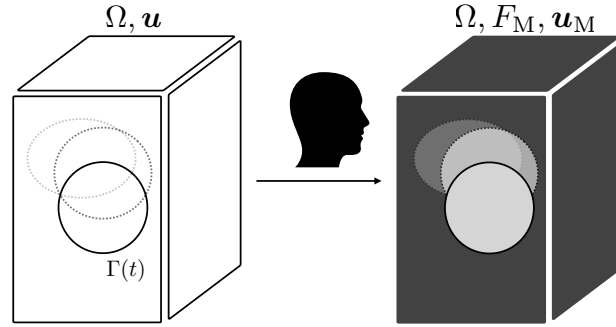


FIGURE 2 The surface $\Gamma(t)$ is transported by \mathbf{u} within the domain Ω . $\Gamma(t)$ is sufficiently visible on the image sequences F_M and \mathbf{u}_M is a measurement of the velocity field \mathbf{u} .

2.1 | The position observation operator from grayscale images

An observation operator of the unknown mapping ϕ from the image data F_M is proposed in this section. Grayscale intensity images of the domain Ω provide geometrical information on the location of the surface $\Gamma(t)$. In fact, moving objects on images are usually visible and trackable to the naked eyes, at least in cases in which there is sufficient intensity contrast, and provided that there is reasonable prior information on the position and the shape. The ability to track the surface motion is a consequence of the fact that the contour, which identifies $\Gamma(t)$, is associated with a *local* extremal value of the norm of the gradient of the image intensity. This property is widely used in basic edge detection techniques. Different image filters have been developed in order to quantify the gradient of the image intensity^{21,22} and thus facilitate contour segmentation. Among them, the Canny edge detection²³ proposes contour identification, since it selects candidate contours given ribbons of extremal gradient. This filter can be limited by the image contrast, and also local inhomogeneities of image intensity inside a coherent region due to image noise, or simply the imaging technique itself. It might thus result in artefacts in the segmentation and non-smooth geometry reconstruction. This shows that maximizing the gradient of the image intensity does not guarantee the regularity of the boundary, even if the boundary of the real object is smooth. For this reason, a regularizing constraint is also added in the surface position operator that will be presented.

In what follows, $\langle \cdot, \cdot \rangle$ denotes the euclidean scalar product and $\| \cdot \|$, the induced norm. From now on, the space of positive-definite symmetric matrices is referred to as $S_d(\mathbb{R})$. An element $B \in S_d(\mathbb{R})$ can be used to define a scalar product: $\langle x, y \rangle_B = \mathbf{x}^T B^{-1} \mathbf{y}$, and the induced norm writes $\| \cdot \|_B$. For each $t \in]0, T]$, the proposed position observation operator involves the minimization of the following functional \mathcal{J}_t , defined for sufficiently regular deformation maps $\psi : \Gamma_R \rightarrow \mathbb{R}^d$:

$$\mathcal{J}_t(\psi) = \frac{1}{2} \int_{\Gamma_R} \left(-\| \nabla_x F_M(\psi(\xi), t) \|_{B_{\text{img}}}^2 + \| \psi(\xi) - \tilde{\phi}(\xi, t) \|_{B_{\text{prior}}}^2 + \delta \| \nabla_\xi (\psi - \tilde{\phi}_0)(\xi) \|^2 \right) d\xi. \quad (2)$$

Here, the symbols ∇_x , ∇_ξ denote the gradient with respect to the cartesian and the curvilinear coordinates, respectively. The mapping $\tilde{\phi}$ represents a prior on the unknown mapping ϕ , so that the second term defines a trust region. The mapping $\tilde{\phi}_0 :=$

$\tilde{\phi}(\cdot, 0)$ accounts for a prior on ϕ_0 . The matrices B_{img} and B_{prior} , both in $S_d(\mathbb{R})$, weigh the confidence in the image gradient term, and the confidence in the prior information, respectively. In practice, we have

$$B_{\text{img}} := \frac{\gamma}{\|\nabla_x F_M(\cdot, t)\|_\infty^2} \mathbf{I}_d,$$

with \mathbf{I}_d the identity matrix in dimension d , $\gamma > 0$ a dimensionless user-defined parameter. B_{prior} is a diagonal matrix whose coefficients are given by the spacings of the image in its three spatial directions. The larger γ , the more confidence is given to the image gradient maximization. The third term of (2) is a regularization term penalizing the norm of the derivatives of the map $\psi - \tilde{\phi}_0$. The position observation is thus defined as $\psi_M : \Gamma_R \times [0, T] \rightarrow \mathbb{R}^d$ such that

$$\psi_M(\cdot, t) := \arg \inf_{\psi} \mathcal{J}_t(\psi(\cdot)) \quad (3)$$

for all $t \in]0, T]$. Minimizing \mathcal{J}_t is equivalent to selecting a smooth surface among all possible surfaces resulting from the local maximization of the image gradient around $\tilde{\phi}$, see Figure 3.

The Euler-Lagrange equations yield the following necessary condition satisfied by ψ_M :

$$-\nabla_{xx} F_M(\psi_M) B_{\text{img}}^{-1} \nabla_x F_M(\psi_M) + B_{\text{prior}}^{-1} (\psi_M - \tilde{\phi}) - \delta \Delta_\xi (\psi_M - \tilde{\phi}_0) = \mathbf{0}, \quad (4)$$

where the symbol $\nabla_{xx} F_M$ denotes the Hessian matrix of F_M .

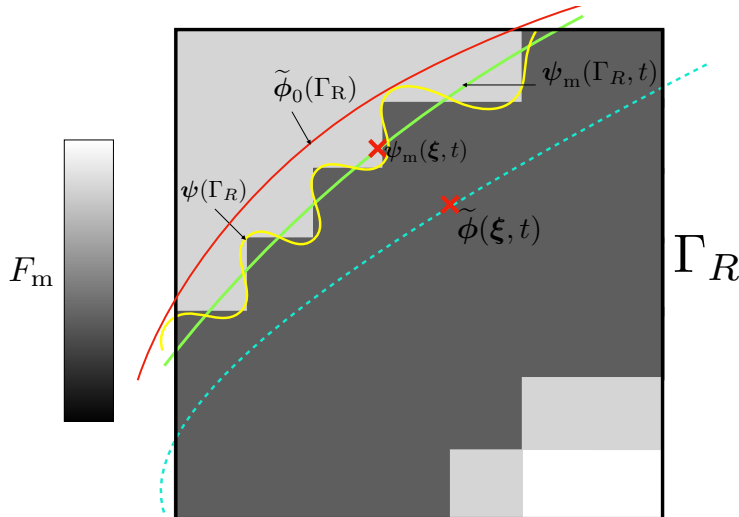


FIGURE 3 The position observer. On the image at $t \in [0, T]$, the maximization of the norm of the image gradient would result in the map ψ with high local curvature. Among all those maps, the regularizing constraint selects ψ_M .

Remark 1. As stated, the position observation operator behaves like an active contour method. The functional \mathcal{J}_t can be decomposed into an image-based energy, given by the two first terms, and an internal energy with the norm of the surface gradient. \square

Obtaining the observed mapping ψ_M directly from (4) would require to treat the non-linearity induced by the image gradient and Hessian term. In what follows, we propose a splitting procedure which mitigates the difficulties encountered either in a direct minimization of \mathcal{J}_t or in the resolution of the Euler-Lagrange equations. Note that the two first terms of \mathcal{J}_t in (2) treat independently points on $\psi(\Gamma_R)$ while the third couples nearby points on the surface. The proposed two-step approach reads as follows:

1. Minimization of a simplified cost functional $\tilde{\mathcal{J}}_t$ to generate an intermediate observation $\tilde{\psi}_M$:

$$\tilde{\psi}_M(\cdot, t) := \arg \inf_{\psi} \tilde{\mathcal{J}}_t(\psi(\cdot)), \quad (5)$$

with

$$\tilde{\mathcal{J}}_t : \boldsymbol{\psi} \rightarrow \frac{1}{2} \int_{\Gamma_R} \left(-\|\nabla_x F_M(\boldsymbol{\psi}(\boldsymbol{\xi}), t)\|_{\mathbf{B}_{\text{img}}}^2 + \|\boldsymbol{\psi}(\boldsymbol{\xi}) - \tilde{\boldsymbol{\phi}}(\boldsymbol{\xi}, t)\|_{\mathbf{B}_{\text{prior}}}^2 \right) d\boldsymbol{\xi}. \quad (6)$$

2. Surface regularization that provides the end-of-step position observation $\boldsymbol{\psi}_M$:

$$\boldsymbol{\psi}_M - \tilde{\boldsymbol{\psi}}_M - \delta \Delta_\xi (\boldsymbol{\psi}_M - \tilde{\boldsymbol{\phi}}_0) = \mathbf{0}. \quad (7)$$

Some remarks are in order to motivate the above splitting approach as an alternative to (3). We have $\mathcal{J}_t = \tilde{\mathcal{J}}_t + \mathcal{G}$, with

$$\mathcal{G} : \boldsymbol{\psi} \rightarrow \frac{1}{2} \int_{\Gamma_R} \delta \|\nabla_\xi (\boldsymbol{\psi} - \tilde{\boldsymbol{\phi}}_0)(\boldsymbol{\xi})\|^2 d\boldsymbol{\xi}.$$

The intermediate position observation $\tilde{\boldsymbol{\psi}}_M$ returned by (5) does not satisfy *a priori* the optimality condition for \mathcal{J}_t , that is, $\partial_\psi \mathcal{J}_t(\boldsymbol{\psi}'_M) \neq \mathbf{0}$. Consequently, a descent gradient method would suggest to move in the opposite direction of the gradient of \mathcal{J}_t , namely, $-\delta(\partial_\psi \tilde{\mathcal{J}}(\tilde{\boldsymbol{\psi}}_M) + \partial_\psi \mathcal{G}(\tilde{\boldsymbol{\psi}}_M)) = -\delta \partial_\psi \mathcal{G}(\boldsymbol{\psi}'_M)$, where here δ plays the role of the step parameter. This step improves $\tilde{\boldsymbol{\psi}}_M$ as minimizer of \mathcal{J}_t , provided that δ is sufficiently small. The second step (7) performs such a gradient descent step from $\tilde{\boldsymbol{\psi}}_M$, but with an implicit treatment of $\boldsymbol{\psi}_M$ in the Frechet derivate term $\partial_\psi \mathcal{G}$.

2.2 | State estimation

We introduce, first, a classical variational formulation of the problem of state estimation. The misfit function reads:

$$\frac{1}{2} \int_0^T \int_{\Gamma_R} \left(\|\boldsymbol{\psi}_M - \boldsymbol{\varphi}\|_{\mathbf{B}_{\text{pos}}}^2 + \|\mathbf{u}_M(\boldsymbol{\psi}_M) - \mathbf{v}\|_{\mathbf{B}_{\text{vel}}}^2 \right) d\boldsymbol{\xi} \quad (8)$$

where $\boldsymbol{\varphi} : \Gamma_R \times [0, T] \rightarrow \mathbb{R}^d$ and $\mathbf{v} : \Gamma_R \times [0, T] \rightarrow \mathbb{R}^d$ satisfy a regularized version of the dynamics (1)

$$\begin{cases} \partial_t \boldsymbol{\varphi}(\boldsymbol{\xi}, t) = \mathbf{v}(\boldsymbol{\xi}, t), & (\boldsymbol{\xi}, t) \in \Gamma_R \times]0, T], \\ \partial_t \mathbf{v}(\boldsymbol{\xi}, t) = \kappa \Delta_\xi (\boldsymbol{\varphi}(\boldsymbol{\xi}, t) - \tilde{\boldsymbol{\phi}}_0(\boldsymbol{\xi})), & (\boldsymbol{\xi}, t) \in \Gamma_R \times]0, T], \\ \boldsymbol{\varphi}(\boldsymbol{\xi}, 0) = \tilde{\boldsymbol{\phi}}_0(\boldsymbol{\xi}), \quad \mathbf{v}(\boldsymbol{\xi}, 0) = \tilde{\mathbf{v}}_0(\boldsymbol{\xi}), & \boldsymbol{\xi} \in \Gamma_R, \end{cases} \quad (9)$$

$\tilde{\boldsymbol{\phi}}_0 : \Gamma_R \rightarrow \mathbb{R}^d$ and $\tilde{\mathbf{v}}_0 : \Gamma_R \rightarrow \mathbb{R}^d$ denote the initial conditions and play the role of a control on the $\boldsymbol{\varphi}$ and \mathbf{v} , in order to reach the optimum in (8). Consequently, the misfit functional (8) depends on the initial condition $(\tilde{\boldsymbol{\phi}}_0, \tilde{\mathbf{v}}_0)$ through (9). Note that, since (1) does not provide any spatial regularity to \mathbf{v} , an elastic regularization (9)₂ has been added. The matrices $\mathbf{B}_{\text{pos}}, \mathbf{B}_{\text{vel}} \in \mathcal{S}_3(\mathbb{R})$ have two purposes. First, they ensure dimensionless comparison between the misfit to the position observation and the misfit to the velocity observation. Second, \mathbf{B}_{pos} and \mathbf{B}_{vel} quantify the confidence in the observed mapping $\boldsymbol{\psi}_M$ and in the observed velocity $\mathbf{u}_M(\boldsymbol{\psi}_M)$, respectively. Hence, the optimization problem:

$$\min_{\tilde{\boldsymbol{\phi}}_0, \tilde{\mathbf{v}}_0} \frac{1}{2} \int_0^T \int_{\Gamma_R} \left(\|\boldsymbol{\psi}_M - \boldsymbol{\varphi}\|_{\mathbf{B}_{\text{pos}}}^2 + \|\mathbf{u}_M(\boldsymbol{\psi}_M) - \mathbf{v}\|_{\mathbf{B}_{\text{vel}}}^2 \right) d\boldsymbol{\xi} dt, \quad (10)$$

such that

$$\begin{cases} \partial_t \boldsymbol{\varphi} = \mathbf{v}, \\ \partial_t \mathbf{v} = \mathcal{F}(\boldsymbol{\varphi}), \\ \boldsymbol{\varphi}(\cdot, 0) = \tilde{\boldsymbol{\phi}}_0(\cdot) \quad \mathbf{v}(\cdot, 0) = \tilde{\mathbf{v}}_0(\cdot), \end{cases} \quad (11)$$

and with $\mathcal{F}(\boldsymbol{\varphi}) := \kappa \Delta_\xi (\boldsymbol{\varphi} - \tilde{\boldsymbol{\phi}}_0)$.

The state estimation is presented as a space and time continuous optimization problem controlled by the initial condition. We propose a method to solve the space and time discretized problem in the following sections.

2.3 | Space discretization

We detail here the discretization of the continuous problem and the position observation operator introduced in Sections 2.2 and 2.1, respectively.

The surface $\Gamma(t)$ is discretized by means of a triangular mesh with N_p points (or landmarks). The landmarks are uniquely identified by their indices $i \in \{0, \dots, N_p - 1\}$ and the motion of the surface $\Gamma(t)$ is assessed through the time-dependent positions $\{\mathbf{q}_i : [0, T] \rightarrow \mathbb{R}^d\}_{i=0, \dots, N_p-1}$ of the landmarks. Let introduce the vector position $\mathbf{Q}(t) = (\mathbf{q}_0(t)^T \cdots \mathbf{q}_{N_p-1}(t)^T)^T \in \mathbb{R}^{dN_p}$. Let $\mathbf{U}(t) = (\mathbf{u}_0(t)^T \cdots \mathbf{u}_{N_p-1}(t)^T)^T \in \mathbb{R}^{dN_p}$ denote the velocity vector of the landmarks such that for all $i \in \{0, \dots, N_p - 1\}$, $\mathbf{u}_i(t) := \partial_t \mathbf{q}_i(t)$ is the velocity of the landmark i , located at $\mathbf{q}_i(t)$ at time t .

Provided that an initial position $\tilde{\mathbf{Q}}^0 := (\tilde{\mathbf{q}}_0^0 \cdots \tilde{\mathbf{q}}_{N_p-1}^0)^T \in \mathbb{R}^{dN_p}$ of the landmarks is specified, the discretized dynamics writes as follow:

$$\begin{cases} \dot{\mathbf{Q}} = \mathbf{U}, \\ \dot{\mathbf{U}} = \kappa \mathbf{K} (\mathbf{Q} - \tilde{\mathbf{Q}}^0), \end{cases} \quad (12)$$

The discrete counterpart of the surface Laplacian is given the interaction matrix $\kappa \mathbf{K}$. We chose a spring-mass model, known to ensure mesh correctness in case of large deformation²⁴. A finite element approximation could have been considered as well. The positive scalar κ is the elasticity parameter. Let us introduce the state of the system

$$\mathbf{X} := \begin{pmatrix} \mathbf{Q} \\ \mathbf{U} \end{pmatrix} \in \mathbb{R}^{2dN_p}$$

The spatially discretized model thus writes:

$$\dot{\mathbf{X}}(t) = \mathbf{A} (\mathbf{X}(t) - \tilde{\mathbf{X}}^0), \quad (13)$$

with

$$\mathbf{A} := \begin{pmatrix} \mathbf{0} & \mathbf{I}_{dN_p} \\ -\mathbf{K}(\kappa) & \mathbf{0} \end{pmatrix} \in \mathbb{R}^{2dN_p \times 2dN_p}, \quad \tilde{\mathbf{X}}^0 := \begin{pmatrix} \tilde{\mathbf{Q}}^0 \\ \mathbf{0} \end{pmatrix} \in \mathbb{R}^{2dN_p}.$$

For $\mathbf{R} := \begin{pmatrix} \mathbf{0} \\ \kappa \mathbf{K} \tilde{\mathbf{Q}}^0 \end{pmatrix} \in \mathbb{R}^{2dN_p}$, it yields equivalently:

$$\dot{\mathbf{X}}(t) = \mathbf{A} \mathbf{X}(t) + \mathbf{R}. \quad (14)$$

2.3.1 | Discrete observation operator

The continuous position operator (5) and (7) is also discretized, so as to provide the position observation of the landmarks. First, as for 4D MRI, the image sequences F_M and the measurement of the velocity \mathbf{u}_M are assumed to be piecewise constant on a voxel grid of size $N_1 \times \cdots \times N_d$. In what follows, the voxels are denoted by Ω_α and are uniquely identified by the multi-index $\alpha = (\alpha_1, \dots, \alpha_d) \in \llbracket 1, N_1 \rrbracket \times \cdots \times \llbracket 1, N_d \rrbracket$, as in the blue annotations in Figure 4 ($d = 2$).

The gradient of F_M is approximated voxel-wise by means of a centered finite differences scheme. The values of F_M and $\nabla_{\mathbf{x}} F_M$ are taken constant per voxel. The voxel values of \mathbf{u}_M are assigned to voxel centers, and whenever we need to estimate them in a generic point $\mathbf{x} \in \Omega$, we will make use of a trilinear interpolation. Then, the prior $\tilde{\phi}(\cdot, t)$ on the surface position is replaced by the prior $\{\tilde{\mathbf{q}}_j(t)\}_{j=0, \dots, N_p}$ on the landmark positions.

The position observation operator is computed by means of the two-stepped approach as in Section 2.1:

Step 1. A cost functional $J_i(\tilde{\mathbf{q}}_i(t); \cdot)$ is minimized on a local window search for each landmark i to generate an intermediate observed position $\mathbf{q}_i^{M^-}(t)$, given the prior position $\tilde{\mathbf{q}}_i(t)$. The landmarks are treated independently since the continuous cost functional (6) does not explicitly couple the position of points on the surface. The voxel window search for the minimization is introduced through the compact notation

$$B(\mathbf{k}, L) = \{ \alpha = (\alpha_1, \dots, \alpha_d) \text{ s.t. } |k_j - \alpha_j| \leq L \}$$

with $L < \min_{k_d} \{(N_{k_d} - 1)/2\}$, and represents the set of voxel indices within the box centered in the voxel $\Omega_{\mathbf{k}}$, of size $(2L + 1)$ in each direction. Let denote $\boldsymbol{\pi} : \Omega \rightarrow \llbracket 1, N_1 \rrbracket \times \cdots \times \llbracket 1, N_d \rrbracket$ the function which associates to each point $\mathbf{x} \in \Omega$, the multi-index \mathbf{k}^* of the voxel strictly containing \mathbf{x} . The minimization is performed by evaluating the cost functional on the centers \mathbf{c}_α of the voxels Ω_α . Hence, the intermediate observed position $\mathbf{q}_i^{M^-}(t)$ is given by $\mathbf{q}_i^{M^-}(t) := \mathbf{c}_{\mathbf{k}^*}$ with

$$\mathbf{k}^* := \arg \min_{\mathbf{k} \in B(\boldsymbol{\pi}(\tilde{\mathbf{q}}_i(t)), \Delta N)} J_i(\tilde{\mathbf{q}}_i(t); \mathbf{c}_{\mathbf{k}}), \quad (15)$$

and

$$J_i(\tilde{\mathbf{x}}; \cdot) : \Omega \rightarrow \mathbb{R}$$

$$\mathbf{x} \mapsto -\gamma \left(\frac{\|\nabla_{\mathbf{x}} F_M(\mathbf{x}, t)\|}{\|\nabla_{\mathbf{x}} F_M(t)\|_{\infty}} \right)^2 + \|\mathbf{x} - \tilde{\mathbf{x}}\|_{B_{\text{prior}}}^2. \quad (16)$$

For each landmark i , the voxel indexed by $\pi(\tilde{\mathbf{q}}_i(t))$ defines the center of the voxel window search. As shown in Figure 4, the local window search of size $2\Delta N + 1$, delimited by a red box, restricts the minimization to a set of voxel centers (in green). $B_{\text{prior}} \in \mathcal{S}_d(\mathbb{R})$ is the same as in the space continuous problem, see Section 2.1.

Step 2. The end-of-step observation $\mathbf{q}_i^M(t)$ is computed by applying the discrete regularization:

$$\mathbf{Q}^M(t) - \mathbf{Q}^{M-}(t) = -\delta \mathbf{K}_{\text{obs}} \cdot (\mathbf{Q}^M(t) - \tilde{\mathbf{Q}}^0), \quad (17)$$

with $\mathbf{Q}^M(t) = (\mathbf{q}_0^M(t) \cdots \mathbf{q}_{N_p-1}^M(t))^T \in \mathbb{R}^{dN_p}$, $\mathbf{Q}^{M-}(t) = (\mathbf{q}_0^{M-}(t) \cdots \mathbf{q}_{N_p-1}^{M-}(t))^T \in \mathbb{R}^{dN_p}$ and $\mathbf{K}_{\text{obs}} := \kappa_{\text{obs}} \mathbf{K} \in \mathbb{R}^{dN_p \times dN_p}$. The diffusion step (17) is performed with the same discretization as introduced in Section 2.3.

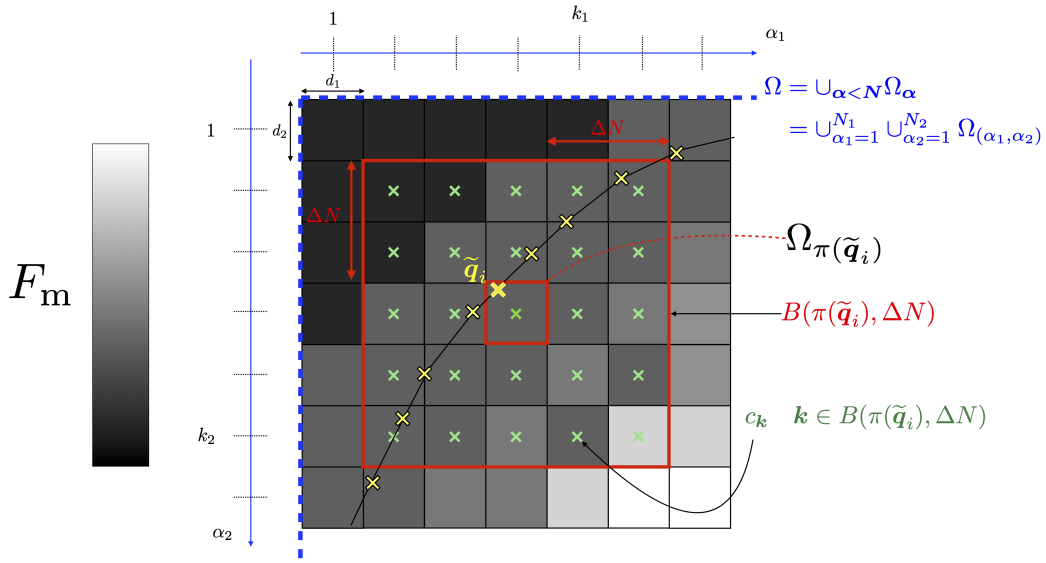


FIGURE 4 Two-dimensional illustration of the optimization step in the position observation operator ($\Delta N = 2$).

The complete state observation $\mathbf{Z} \in \mathbb{R}^{2dN_p}$ is thus given by

$$\mathbf{Z}(t) = \begin{pmatrix} \mathbf{Q}^M(t) \\ \mathbf{U}^M(t) \end{pmatrix},$$

with $\mathbf{U}^M(t) = (\mathbf{u}_M(\mathbf{q}_0^M(t), t)^T \cdots \mathbf{u}_M(\mathbf{q}_{N_p-1}^M(t), t)^T)^T \in \mathbb{R}^{dN_p}$. In what follows, we shall use the abstract notation:

$$\mathbf{Z}(t) = \mathcal{F}_{\text{obs}} \left(F_M(\cdot, t), \mathbf{u}_M(\cdot, t), \tilde{\mathbf{Q}}(t), \gamma, \Delta N, \delta, \kappa_{\text{obs}} \right), \quad (18)$$

for the observation operator.

2.4 | Time discretization: fully discrete formulation

In real applications, both image sequences and the eulerian velocity field \mathbf{u}_M are sampled at equally distributed times over the interval $[0, T]$. We thus introduce the time discretization.

For $N_T \in \mathbb{N}^*$, let $N_T + 1$ be the number of samples available, so that $\Delta T := T/N_T$ denotes the time resolution of the images and the measured velocity. The image sequences and the velocity measurement are acquired at the same time. For $n = 0, \dots, N_T$,

The principle is the following: dynamical equations of the system are available and also some observed quantities. If there were a perfect knowledge of the the dynamics, the state would be perfectly determined from the initial condition. In the practice there may be uncertainties in the initial condition, and sometimes a lack of knowledge in the dynamical equations. The observation are expected to compensate those uncertainties. In the case of our problem, the initial condition is unknown, and a reference configuration serves as initial prior. In addition, at regular time intervals, linear state observations of the system are provided. Kalman filter combines the information from the background value, the prescribed model and the state observation to provide an optimal state estimation in the sense of the minimization of the discrepancy to the observation weighed by the error covariances. It yields an optimal compromise given the uncertainty on the initial state, the model error, the state observation error.

The Kalman filter will be directly applied to our specific case. Minor features are introduced compared to a more generic presentation²⁶. As a first step, the observation is assumed given at the beginning of iteration n . After presenting the filter, the method to generate that observation will be detailed.

Initialization

A prior initial state $\hat{\mathbf{X}}^0 = (\hat{\mathbf{Q}}^0 \ \hat{\mathbf{U}}^0)^T \in \mathbb{R}^{2dN_p}$ is required with its error covariance matrix $\mathbf{P}_0 \in \mathbb{R}^{2dN_p \times 2dN_p}$. It means that the prior can be expressed as $\mathbf{X}^0 + \boldsymbol{\eta}^0$, with $\mathbf{X}^0 = \mathbf{X}(0)$ the real initial state, and $\boldsymbol{\eta}^0$ a noise such that $\mathbb{E}[\boldsymbol{\eta}^0] = \mathbf{0}$ and of $\mathbb{E}[(\boldsymbol{\eta}^0)^T(\boldsymbol{\eta}^0)] = \mathbf{P}_0$. $\hat{\mathbf{Q}}^0$ defined the prior on the initial position the landmarks. $\hat{\mathbf{U}}^0$ is their associated initial velocity, set to $\hat{\mathbf{U}}^0 = \mathbf{0}$, with a large uncertainty with respect to the variable \mathbf{U} in \mathbf{P}_0 . Consequently,

$$\hat{\mathbf{X}}^0 = \begin{pmatrix} \hat{\mathbf{Q}}^0 \\ \mathbf{0} \end{pmatrix}.$$

Prediction

At t_n , given the best current state estimation $\hat{\mathbf{X}}^{n-1} = (\hat{\mathbf{Q}}^{n-1} \ \hat{\mathbf{U}}^{n-1})^T$, a prediction $\hat{\mathbf{X}}^{n-}$ is computed from the model. The *a priori* covariance matrix \mathbf{P}_{n-} is computed. The sampling time step and the integration time step are assumed equal.

$$\begin{cases} \hat{\mathbf{X}}^{n-} = \mathbf{D}_{n-1|n} \hat{\mathbf{X}}^{n-1} + \mathbf{R}^n, \\ \mathbf{P}_{n-} = \mathbf{D}_{n-1|n} \mathbf{P}_{n-1} \mathbf{D}_{n-1|n}^T. \end{cases} \quad (24)$$

Since the model is not perfect, a model error is included in the computation of the prediction covariance matrix. Let $\mathbf{W}_{\text{model}} \in \mathbb{R}^{2dN_p \times 2dN_p}$ be the model error covariance matrix in 1. The update of the prediction covariance matrix (26)₂ becomes

$$\mathbf{P}_{n-} = \mathbf{D}_{n-1|n} \mathbf{P}_{n-1} \mathbf{D}_{n-1|n}^T + \mathbf{W}_{\text{model}}.$$

Correction

The Kalman correction due to the discrepancy between the model prediction $\hat{\mathbf{X}}^{n-}$ and the observation \mathbf{Z}^n is computed as $\mathbf{K}_n(\mathbf{Z}^n - \hat{\mathbf{X}}^{n-})$. $\mathbf{K}_n \in \mathbb{R}^{2dN_p \times 2dN_p}$ is the Kalman gain matrix and $\mathbf{Z}^n - \hat{\mathbf{X}}^{n-}$ is often called the innovation vector. The covariance matrix $\mathbf{W}_{\text{obs}} \in \mathbb{R}^{2dN_p \times 2dN_p}$ quantifies the uncertainty in the observation. It is mainly expressed from the precision of the position observer, and the noise in the measured velocity. The most expensive part of the correction step is the calculation of \mathbf{K}_n in Algorithm 1. In a vast majority of application cases of Kalman filter, \mathbf{K}_n is of smaller size since the observation is of lower dimension than the state. Here calculating \mathbf{K}_n requires increased memory and computational time. The covariance matrix \mathbf{P}_n associated to the estimation quantifies the error on the estimation $\hat{\mathbf{X}}^n$ that is returned at time t_n . $\hat{\mathbf{X}}^n$ will be the prior at the beginning of the next iteration.

3.2 | Proposed estimation algorithm

Implicit-Explicit model prediction

The model dynamics (14) is integrated using a Backward Euler time-stepping scheme to generate the prediction. It induces subsequent update of the prediction matrix:

$$\begin{cases} \mathbf{B}_{n-1|n} \hat{\mathbf{X}}^{n-} = \hat{\mathbf{X}}^{n-1} + \mathbf{R}^n, \\ \mathbf{P}_{n-} = \mathbf{B}_{n-1|n}^{-1} \mathbf{P}_{n-1} \mathbf{B}_{n-1|n}^{-T} + \mathbf{W}_{\text{model}}, \end{cases} \quad (25)$$

with $\mathbf{B}_{n-1|n} = \mathbf{I}_{2dN_p} - \Delta T \cdot \mathbf{A} \in \mathbb{R}^{2dN_p \times 2dN_p}$, \mathbf{I}_{2dN_p} being the identity matrix of size $2dN_p \times 2dN_p$ and $\mathbf{R}^n = \Delta T \cdot \mathbf{R} \in \mathbb{R}^{2dN_p}$. Inverting the system (25)₁ does not require to compute the inverse of $\mathbf{B}_{n-1|n}$, while the update of the covariance matrix does. Inverting the matrix $\mathbf{B}_{n-1|n}$ could turn out to be prohibitive given the size of the mesh considered in the application. One possible

Algorithm 1 (Simplified) Linear Kalman Filter

Require: $(\hat{\mathbf{X}}^0; \mathbf{P}_0)$, $(\mathbf{A}_{n-1|n}, \mathbf{R}_{n=0, \dots, N_T}; \mathbf{W}_{\text{model}})$, $(\mathbf{Z}^n; \mathbf{W}_{\text{obs}})$
for $n = 1, \dots, N_T$ **do**
 Prediction: $(\hat{\mathbf{X}}^{n-1}, \mathbf{P}_{n-1}) \rightarrow (\hat{\mathbf{X}}^{n^-}, \mathbf{P}_{n^-})$
 $\hat{\mathbf{X}}^{n^-} \leftarrow \mathbf{D}_{n-1|n} \hat{\mathbf{X}}^{n-1} + \mathbf{R}^n$
 $\mathbf{P}_{n^-} \leftarrow \mathbf{D}_{n-1|n} \mathbf{P}_{n-1} \mathbf{D}_{n-1|n}^T + \mathbf{W}_{\text{model}}$
 Correction: $(\mathbf{Z}^n, \mathbf{W}_{\text{obs}}, \hat{\mathbf{X}}^{n^-}, \mathbf{P}_{n^-}) \rightarrow (\hat{\mathbf{X}}^n, \mathbf{P}_n)$
 $\mathbf{S}_n \leftarrow \mathbf{P}_{n^-} + \mathbb{W}_{\text{obs}}$
 \mathbf{K}_n^T is solution of $\mathbf{S}_n^T \boldsymbol{\chi} = \mathbf{P}_{n^-}^T$
 $\hat{\mathbf{X}}^n \leftarrow \hat{\mathbf{X}}^{n^-} + \mathbf{K}_n (\mathbf{Z}^n - \hat{\mathbf{X}}^{n^-})$
 $\mathbf{P}_n \leftarrow (\mathbf{I} - \mathbf{K}_n) \mathbf{P}_{n^-}$
end for
return $(\hat{\mathbf{X}}^n, \mathbf{P}_n)$, $n = 1, \dots, N_T$

alternative is to update the covariance matrix as in case of a forward Euler (26)₂. We will systematically use that option, called in the paper *implicit-explicit prediction*. A forward Euler time scheme applied to the model (14) would return the following time discretization of the model:

$$\begin{cases} \hat{\mathbf{X}}^n = \mathbf{A}_{n-1|n} \hat{\mathbf{X}}^{n-1} + \mathbf{R}^n, \\ \mathbf{P}_{n^-} = \mathbf{A}_{n-1|n} \mathbf{P}_{n-1} \mathbf{A}_{n-1|n}^T + \mathbf{W}_{\text{model}}, \end{cases} \quad (26)$$

with $\mathbf{A}_{n-1|n} = \mathbf{I}_{2dN_p} + \Delta T \cdot \mathbf{A} \in \mathbb{R}^{2dN_p \times 2dN_p}$.

Hence, our implicit-explicit prediction writes as follows:

$$\begin{cases} \mathbf{B}_{n-1|n} \mathbf{X}^n = \mathbf{X}^{n-1} + \mathbf{R}^n, \\ \mathbf{P}_{n^-} = \mathbf{A}_{n-1|n} \mathbf{P}_{n-1} \mathbf{A}_{n-1|n}^T + \mathbf{W}_{\text{model}}. \end{cases} \quad (27)$$

The covariance matrix of the model error $\mathbf{W}_{\text{model}}$ is calculated from the assumption that the model error results from a white noise in acceleration whose covariance matrix is $\sigma_a^2 \mathbf{I}_{dN_p}$. Consequently we propose an approximation² of model error covariance matrix, given by:

$$\mathbf{W}_{\text{model}} = \sigma_a^2 \begin{pmatrix} \frac{\Delta T^4}{4} \mathbf{I}_{dN_p} & \frac{\Delta T^3}{2} \mathbf{I}_{dN_p} \\ \frac{\Delta T^3}{2} \mathbf{I}_{dN_p} & \Delta T^2 \mathbf{I}_{dN_p} \end{pmatrix}. \quad (28)$$

Remark 2. We propose a reasonable order of magnitude for σ_a from the expression of $\mathbf{W}_{\text{model}}(\sigma_a)$. In fact, the noise in acceleration induces an error on the position $\Delta T^2 \sigma_a / 2$ which should be of at least of some voxels spacing $N \sqrt{h_1^2 + \dots + h_d^2}$ to be have a significative effect on the reconstruction compared to the observation error introduced by (15). It yields the approximation

$$\sigma_a \sim 2N \sqrt{h_1^2 + \dots + h_d^2} / \Delta T^2. \quad (29)$$

This only serves as an heuristic approach, which has proven to work for the synthetic test case and the application to real data in Section 4. \square

Generating the prior $\tilde{\mathbf{Q}}^n$

As explained previously, the observation at iteration n depends on $\tilde{\mathbf{Q}}^n$ which is yet to be determined. Since $\tilde{\mathbf{Q}}^n$ is a prior value for the state at iteration n , a reasonable guess could come from the model prediction. Given $\hat{\mathbf{X}}^{n-1}$ the prior for the local maximization of the image gradient is set to $\mathbf{B}_{n-1|n}^{-1} (\hat{\mathbf{X}}^{n-1} + \mathbf{R}^n)$ or equivalently $\mathbf{B}_{n-1|n} \tilde{\mathbf{Q}}^n = \hat{\mathbf{X}}^{n-1} + \mathbf{R}^n$. Consequently, the observation is given by

$$\mathbf{Z}^n = \mathcal{F}_{\text{obs}} \left(\mathbf{F}_{\text{M}}^n, \mathbf{u}_{\text{M}}^n, \mathbf{B}_{n-1|n}^{-1} (\hat{\mathbf{X}}^{n-1} + \mathbf{R}^n), \gamma, \Delta N, \delta, \kappa_{\text{obs}} \right),$$

taking up the notation introduced in Section 2.4. Note that this is an abuse of notation, since $\mathbf{B}_{n-1|n}$ is not inverted and we instead solve the associated linear system.

The Kalman filter requires the user to specify the following parameters:

²This approximation results from the propagation of a noise in acceleration for a zero-acceleration dynamical equation, that is to say $\ddot{\mathbf{q}} = \mathbf{a}$, with \mathbf{a} a white noise.

Algorithm 2 Full algorithm

Require: $(\hat{\mathbf{X}}^0, \mathbf{P}_0)$, $(A_{n-1|n}, \mathbf{R}_{n=0, \dots, N_T}; \mathbf{W}_{\text{model}})$, \mathbf{W}_{obs}
for $n = 1, \dots, N_T$ **do**
 Generate observation $\mathbf{Z}^n = \mathcal{F}_{\text{obs}} \left(F_{\text{M}}^n, \mathbf{B}_{n-1|n}^{-1} \left(\hat{\mathbf{X}}^{n-1} + \mathbf{R}^n \right), \gamma, \Delta N, \delta, \kappa_{\text{obs}} \right)$
 Apply Prediction: $(\hat{\mathbf{X}}^{n-1}, \mathbf{P}_{n-1}) \rightarrow (\hat{\mathbf{X}}^n, \mathbf{P}_{n-})$ from Algorithm 1
 Apply Correction: $(\mathbf{Z}^n, \mathbf{W}_{\text{obs}}, \hat{\mathbf{X}}^n, \mathbf{P}_{n-}) \rightarrow (\hat{\mathbf{X}}^n, \mathbf{P}_n)$ from Algorithm 1
end for
 return $(\hat{\mathbf{X}}^n, \mathbf{P}_n)$, $n = 1, \dots, N_T$

- For the model: $\sigma_a > 0$, directly associated to the norm of $\mathbf{W}_{\text{model}}$ from (28).
- For the observation: $\sigma_q > 0$ and $\sigma_p > 0$, parameters for the covariance matrix $\mathbf{W}_{\text{obs}} \in \mathbb{R}^{2dN_p \times 2dN_p}$:

$$\mathbf{W}_{\text{obs}} = \mathbf{W}_{\text{obs}}(\sigma_q, \sigma_p) = \begin{pmatrix} (\sigma_q \mathbf{D}_{N_p})^2 & 0 \\ 0 & \sigma_p^2 \mathbf{I}_{dN_p} \end{pmatrix}.$$

$\mathbf{D}_{N_p} = \text{diag}(\mathbf{D}, \dots, \mathbf{D}) \in \mathbb{R}^{dN_p \times dN_p}$ denotes the block diagonal matrix defined with the spacing matrix of the image data, $\mathbf{D} = \text{diag}(\delta_0, \dots, \delta_{d-1}) \in \mathbb{R}^{d \times d}$. For $i = 0, \dots, d-1$, δ_i is the image spacing along the i -th axis.

- For the initial configuration: $\sigma_{P_0,q} > 0$ and $\sigma_{P_0,p} > 0$, parameters of the covariance matrix $\mathbf{P}_0 \in \mathbb{R}^{2dN_p \times 2dN_p}$:

$$\mathbf{P}_0 = \mathbf{P}_0(\sigma_{P_0,q}, \sigma_{P_0,p}) = \begin{pmatrix} (\sigma_{P_0,q} \mathbf{D}_{N_p})^2 & 0 \\ 0 & \sigma_{P_0,p}^2 \mathbf{I}_{dN_p} \end{pmatrix}.$$

Unlike σ_p and $\sigma_{P_0,p}$, the user-defined parameters σ_q and $\sigma_{P_0,q}$ are dimensionless and their values represent pixel radius of trust regions. In addition to the Kalman filter parameters, specific parameters must be specified:

- For the model (prediction): the stiffness/elasticity parameter $\kappa \geq 0$.
- For the observation: $\gamma > 0$, $\Delta N \in \mathbb{N}^*$ the size of the local search window. Those parameters will be fixed. Intuitively the values prescribed should depend on the quality of the image. For the elasticity equation: the parameters $\kappa_{\text{obs}} \geq 0$, or rather the product $\kappa_{\text{obs}} \delta \geq 0$.

One can refer to Figure 5 for an overview of the parameters.

4 | NUMERICAL EXPERIMENTS

The purpose of this section is to illustrate the capabilities of Algorithm 2 by means of numerical experiments. The proposed test cases also aim to assess the sensitivity of the method to free parameters (see Tables 1 and 2) and noisy data. We consider two test cases. The first one (Section 4.1) is based on synthetic data and the second (Section 4.2) uses real data from 4D flow MRI exam of a human aorta.

The precision of the surface segmentation is evaluated through the Dice coefficient, a metric used in image segmentation to compare the level of similarity of two segmentations. For \mathcal{X} the ground truth segmentation, and \mathcal{X}' another segmentation, both represented by collections of voxels, the Dice coefficient is given by the relation

$$\text{Dice}(\mathcal{X}, \mathcal{X}') := \frac{\text{card}(\mathcal{X} \cap \mathcal{X}')}{\text{card}(\mathcal{X}) + \text{card}(\mathcal{X}')},$$

where card stands for the cardinality of a set. In the synthetic test case, another complementary approach is proposed to account for the quality of the local tracking.

Algorithm 2 has been implemented using the standard C++ libraries, and the Eigen library for linear algebra operations²⁹. The VTK library has also been intensively used for handling images and geometrical objects³⁰.

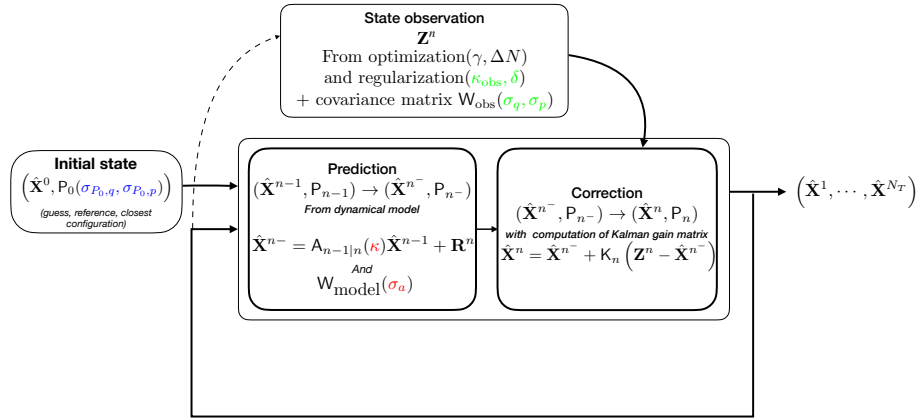


FIGURE 5 The parameters of the Kalman filter and the state observation.

4.1 | Tracking of a vesicle immersed in a lid-driven cavity flow

In this example, we consider the tracking of the motion of an elastic vesicle immersed in a lid-driven cavity flow (see Figure 6). Synthetic image data are generated from numerical simulations of the corresponding dynamical system. In particular, the simulated Eulerian velocity field is extracted so as to mimic 4D MRI flow series. Algorithm 2 is then used to retrieve the motion of the vesicle from the generated synthetic data. We investigate the sensitivity of the reconstruction considering the data quality (image, velocity measurements) and the regularization parameters.

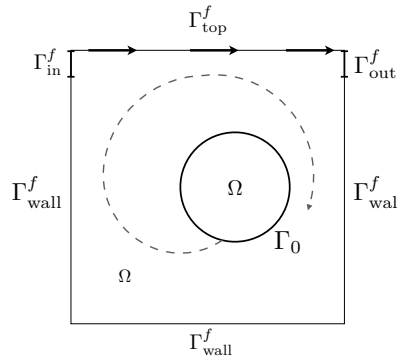


FIGURE 6 Geometrical configuration.

4.1.1 | Data generation.

The considered dynamical system can be modeled by a non-linear fluid-structure interaction model (see, e.g.,³¹ for the details). The fluid is initially at rest and occupies the domain $\Omega := [0, 1] \times [0, 1]$. The vesicle is also initially at rest and has the shape of a circle centered at $(0.6, 0.5)$ with radius 0.2. All the units are given in the CGS system. The fluid is described by the incompressible Navier-Stokes equations, while a non-linear Reissner-Mindlin beam model in Lagrangian formalism is considered for the vesicle. The physical parameters for the fluid are: $\rho^f = 100$, $\nu = 10$, and for the solid equation $\rho^s = 100$, the Young Modulus $E = 5.6 \times 10^3$ and the Poisson's ratio $\nu = 0.4$. The boundary conditions on $\partial\Omega := \Gamma_{\text{wall}}^f \cup \Gamma_{\text{in}}^f \cup \Gamma_{\text{out}}^f \cup \Gamma_{\text{top}}^f$ (see Figure 6) are the following: no-slip boundary conditions on $\Gamma_{\text{top}}^f \cup \Gamma_{\text{wall}}^f$, zero traction on $\Gamma_{\text{in}}^f \cup \Gamma_{\text{out}}^f$, constant velocity equal to 1 on Γ_{top}^f . Synthetic data has

been generated by simulating 4000 time steps, of length $\Delta T_0 = 5.0 \times 10^{-3}$, using the numerical method proposed in³¹ with a fluid mesh made of 12800 triangular elements and 19360 edges, and a solid mesh made of 160 edges.

Some snapshots of the fluid velocity magnitude and solid deformation are given in Figure 7. The vesicle deforms and rotates within the fluid cavity.

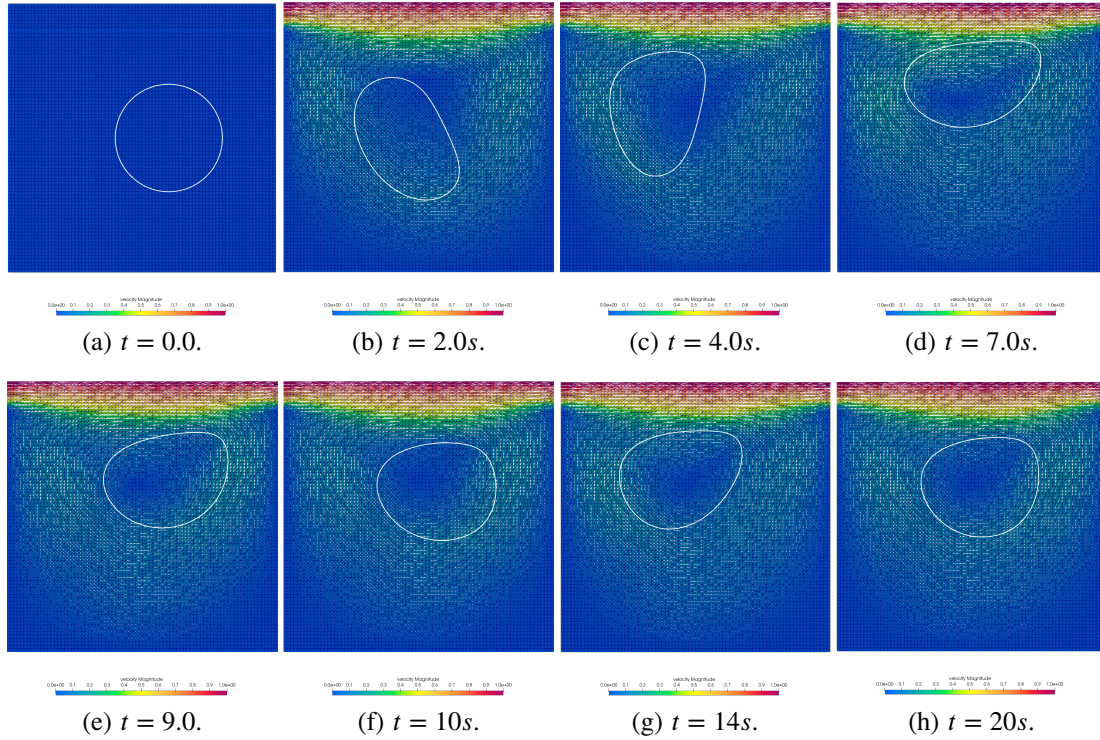


FIGURE 7 Data generation - Motion of the immersed vesicle, from FSI simulations.

From the solid displacement, the grayscale image frames $\{F_M^n\}_{n=0, \dots, N_T-1}$ of the vesicle in motion are generated, with a sampling time length $\Delta T = 20 \times \Delta T_0$, which represents the temporal resolution of the images. It results in $N_T = 200$ image frames. The pixel grid dimension is 80×80 with an isotropic spacing $h_1 = h_2 = 0.0125$. In fact, two adjacent triangles in the mesh of the cavity combine into one square, defining a pixel, as shown in Figure 8. This sets the image resolution. In order to generate the grayscale image at a time-step $n \in \{0, \dots, N_T - 1\}$, we first assign one value among $\{0, 200\}$ to each pixel depending on its location with respect to the vesicle Γ^n . Pixels located inside the vesicle are assigned the maximum value 200, and those strictly outside have a value 0. The resulting binary image $F_{M,0}^n$ at the time step n thus writes

$$F_{M,0}^n : \left\{ \Omega_{\alpha=(\alpha_1, \alpha_2)} \text{ s.t. } (\alpha_1, \alpha_2) \in \llbracket 1, 80 \rrbracket \times \llbracket 1, 80 \rrbracket \right\} \rightarrow \{0, 200\}$$

$$(\Omega_{\alpha}, t) \mapsto \begin{cases} 200, & \text{if } c_{\alpha} \text{ is inside } \Gamma^n \\ 0 & \text{otherwise,} \end{cases} \quad (30)$$

where $\{\Omega_{\alpha}, \alpha \in \llbracket 1, 80 \rrbracket \times \llbracket 1, 80 \rrbracket\}$ is the voxel grid covering Ω , c_{α} the center of a voxel Ω_{α} .

$F_{M,0}^n$ is then blurred to generate a grayscale image $F_{M,1}^n$ using a Gaussian filter implemented in the VTK library `vtkImageGaussianSmooth`³. The filter consists in a convolution with a 2D gaussian kernel⁴ as follows:

$$K_{2D}(i, j) := \frac{1}{2\pi\sigma_1\sigma_2} \exp \left[- \left(\frac{i^2}{2\sigma_1^2} + \frac{j^2}{2\sigma_2^2} \right) \right] = \underbrace{\frac{1}{\sqrt{2\pi}\sigma_1} \exp \left(- \frac{i^2}{2\sigma_1^2} \right)}_{:=K_{1D}^{(1)}(i)} \underbrace{\frac{1}{\sqrt{2\pi}\sigma_2} \exp \left(- \frac{j^2}{2\sigma_2^2} \right)}_{K_{1D}^{(2)}(j)}, \quad (31)$$

for $i \in \{-R_1, -R_1 + 1, \dots, R_1\}$ and $j \in \{-R_2, -R_2 + 1, \dots, R_2\}$, $R_1, R_2 \in \mathbb{N}^*$. For a voxel labelled $\alpha = (\alpha_1, \alpha_2)$, the evaluation of $F_{M,1}^n$ is given by :

$$\begin{aligned} F_{M,1}^n(\alpha_1, \alpha_2) &= [F_{M,0}^n * K_{2D}](\alpha_1, \alpha_2) = \sum_{i=-R_1}^{R_1} \sum_{j=-R_2}^{R_2} F_{M,0}^n(\alpha_1 - i, \alpha_2 - j) K_{2D}(i, j) \\ &= \sum_{i=-R_1}^{R_1} [F_{M,0}^n * K_{1D}^{(2)}](\alpha_1 - i, \alpha_2) K_{1D}^{(1)}(i) \\ &= \sum_{i=-R_2}^{R_2} [F_{M,0}^n * K_{1D}^{(1)}](\alpha_1, \alpha_2 - j) K_{1D}^{(2)}(j), \end{aligned} \quad (32)$$

where $*$ denotes the convolution product. Note the abuse of notation for $F_{M,0}^n, F_{M,1}^n$, since the voxel label is assimilated to the voxel itself. VTK adds a normalization to the gaussian kernel. The kernel size parameters $R_k, k = 1, 2$ depend on the parameters σ_k with the relation $R_k = 2[\sigma_k R'] + 1$, R' being a radius factor. The gaussian blur is performed with $\sigma_1 = \sigma_2 = \sigma$ and $R' = 1$. The standard deviation σ is expressed in pixel units. The main purpose of the gaussian kernel is to reduce the gradient gap across the contours, hence artificially degrading the performance of the image gradient maximization. The larger σ , the more challenging an accurate contour detection might be. Gradient artifacts are finally added to $F_{M,1}^n$, as it may occur with 4DMRI, using a gaussian noise with null-expected value and a standard deviation of 5% of 200, providing the image F_M^n .

The eulerian velocity field \mathbf{u}_M is composed of the exact velocity inside the cavity Ω , with an additive gaussian noise $\boldsymbol{\eta}$ with $\mathbf{0}$ -mean and $\sigma_v^2 \mathbf{I}_2$ covariance matrix. The evaluation of \mathbf{u}_M at any point inside the cavity is approximated by linear interpolation before adding the gaussian noise.

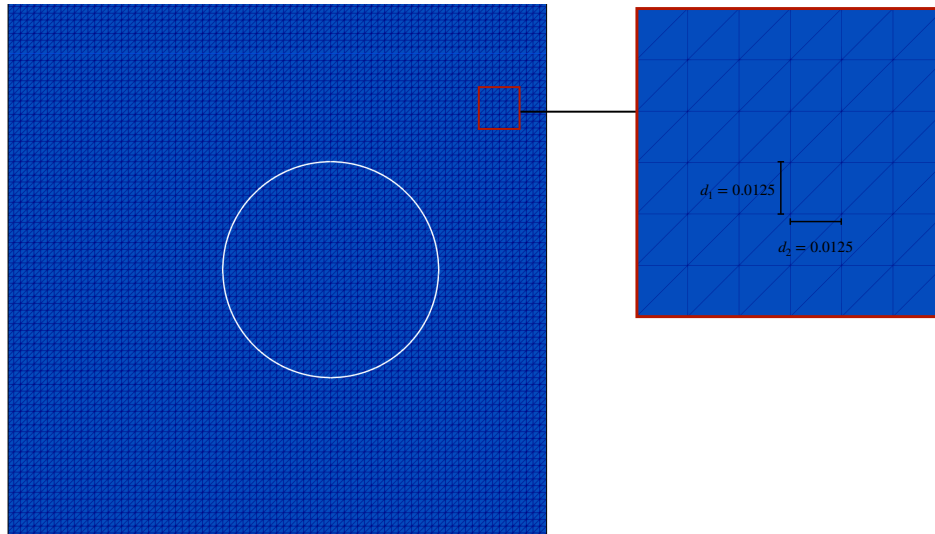


FIGURE 8 Data generation - The mesh of the cavity, with the initial geometrical configuration of the real vesicle.

³Detailed implementation on <https://github.com/Kitware/VTK/blob/master/Imaging/General/vtkImageGaussianSmooth.cxx>

⁴see `vtkImageGaussianSmooth`

Initial configuration

The initial configuration for the tracking is given by a mesh composed of $N_p = 16$ equally distributed points $\{\hat{q}_i^0\}_{i=0,\dots,N_p}$ along an ellipse centered at $(0.65, 0.42)$ of semi-major axis 0.22 and semi-minor axis 0.2, see Figure 9. The center of the ellipse has been translated by a vector $(0.05, -0.08)$ with respect of the center of the real initial configuration. The Dice coefficient at the initialization is 0.72. The time resolution is $\Delta T = 0.1$, $N_T = 200$. A finer time integration is used for the model (27), namely 0.001, as mentioned in Section 3.2.

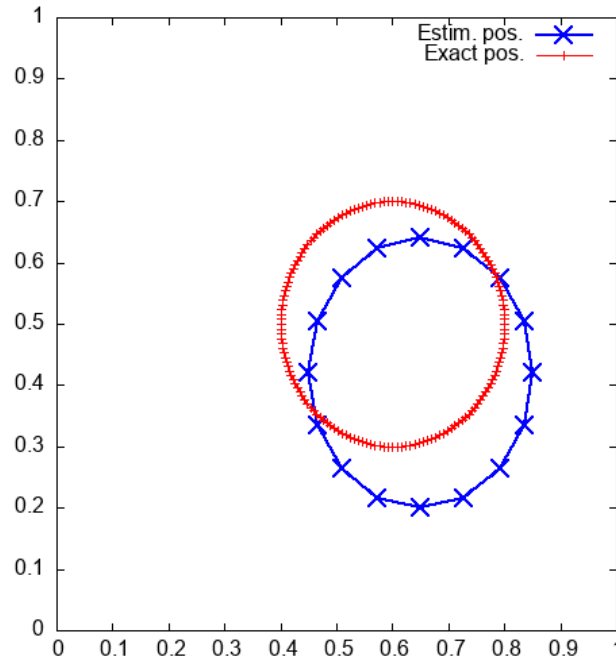


FIGURE 9 Initial configuration. In red, the initial position of the real vesicle. In blue, the initial mesh given to the filter for reconstruction.

4.1.2 | Sensitivity to data quality

Presentation of the test case

The sensitivity of the filter with respect of the level of blur σ in the images is investigated for different values of the velocity noise σ_v . The blur parameter σ controls the diffusion of the gradient extremal values, so that large values of σ makes the observation of the surface position more challenging. The data quality thus depends on σ and σ_v . The parameters of the simulations are given in Table 1.

Parameters	Data quality		Intialization		Model		Observation				
	σ	σ_v	$\sigma_{P_0,q}$	$\sigma_{P_0,p}$	κ	σ_a	γ	ΔN	$\kappa_{\text{obs}} \delta$	σ_q	σ_p
Values	{ 2.0, 6.0 }	{ 0.003, 0.03, 0.075, 0.105 }	$10h_x$	0.1	10	5.0	100	30	0.1	{ 1.5, 2.5, 3.0 }	σ_v

TABLE 1 Parameters for the first synthetic test case.

The simulations are performed with $\sigma = 2.0, 6.0$ (see Figures 10 and 11) and $\sigma_v = 0.003, 0.03, 0.075, 0.105$. The values of σ_v simulate respectively 1%, 10%, 25% and 35% of the half range of variation of the highest component of \mathbf{u}_M^n in an area around the

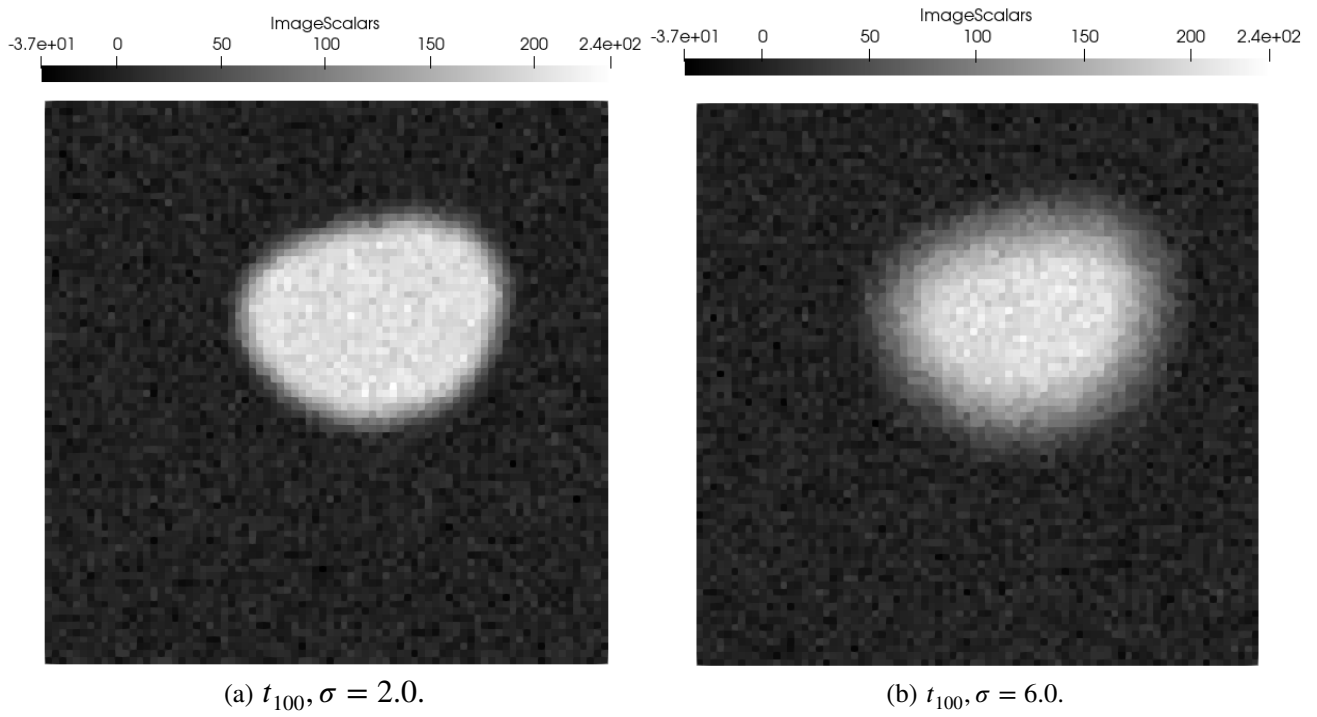


FIGURE 10 Noisy images with $\sigma = 2.0, 6.0$.

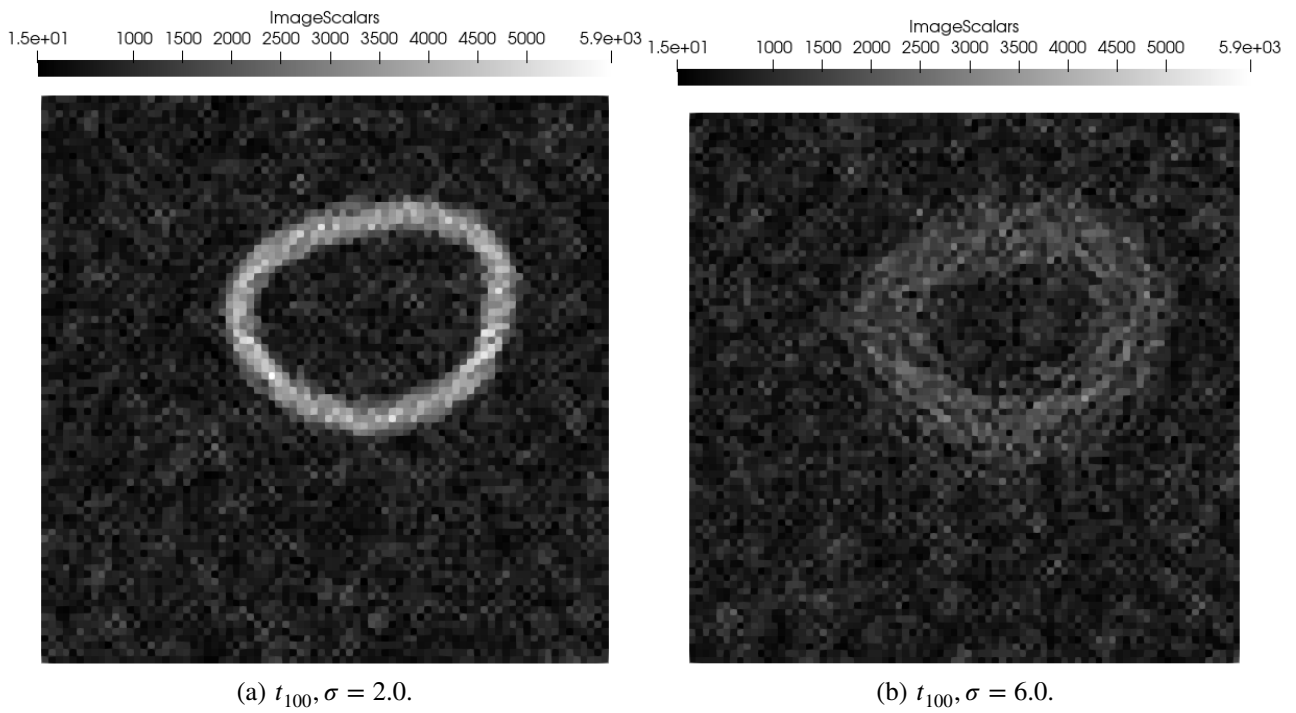


FIGURE 11 Gradient magnitude images with $\sigma = 2.0, 6.0$.

vesicle, for all time steps. Here, that half range corresponds to 0.30. Those percentages deem as an appreciation of the estimated level of noise in the flow series. Depending on the level of blur, the precision σ_q of the position observation operator is adapted

accordingly. For $\sigma = 2.0, 6.0, 8.0$, we respectively set $\sigma_q = 1.5, 2.5, 3.0$. Since every simulation is unique for a set of parameters $(\sigma, \sigma_q, \sigma_v)$, the Dice coefficient is averaged over 100 simulations. For a given triplet of parameters $(\sigma, \sigma_q, \sigma_v)$, every simulation is unique and provides a subsequent evolution of the Dice coefficient over the iterations. 100 simulations are performed for a each set of parameters and the Dice coefficient at each time step is averaged over all the simulations.

In addition to measuring the accuracy of the surface segmentation with the evolution of the dice coefficient, we also check the point-to-point tracking on single simulations. For $n \geq 1$, the exact position of the tracked surface Γ^n is discretized in terms of a set of points $\{\mathbf{q}_j^n\}_{j=0, \dots, N_E}$, and $\{\hat{\mathbf{q}}_i^n\}_{i=0, \dots, N_P}$ denote the estimation provided by Algorithm 2. The quality of the point-to-point tracking of Γ^n by $\{\hat{\mathbf{q}}_i^n\}_{i=0, \dots, N_P}$ is measured by comparing the trajectories of two points whose labels $i_{\min}, i_{\max} \in \{0, \dots, N_P\}$ respectively to the trajectories of $j_{\min}, j_{\max} \in \{0, \dots, N_E\}$. i_{\min}, i_{\max} are defined as follows:

$$i_{\min} := \arg \min_{i \in \{0, \dots, N_P\}} d(\hat{\mathbf{q}}_i^{N_T}, \Gamma^{N_T}), \quad i_{\max} := \arg \max_{i \in \{0, \dots, N_P\}} d(\hat{\mathbf{q}}_i^{N_T}, \Gamma^{N_T}),$$

where the symbol $d(\mathbf{q}, S)$ indicates the distance between the surface S and the point \mathbf{q} . j_{\min} and j_{\max} are the labels of the closed-point projections on Γ^{N_T} of the points $\hat{\mathbf{q}}_{i_{\min}}^{N_T}$, respectively $\hat{\mathbf{q}}_{i_{\max}}^{N_T}$. Note that, the discrete trajectories $\{\hat{\mathbf{q}}_{i_{\min}}^n\}_{n=1, \dots, N_T}$ and $\{\hat{\mathbf{q}}_{i_{\max}}^n\}_{n=1, \dots, N_T}$ respectively represent the best and worst choice for error quantification. When using Kalman filter, the presumably tracked point on Γ^{N_T} by $\{\hat{\mathbf{q}}_i^n\}_{i=0, \dots, N_P}$ can only be assessed at the final iteration. In fact, the linear Kalman filter estimation improves as observations are provided, which makes it the most accurate at final iteration. In the result section, the plots of the discrete trajectories $\{\hat{\mathbf{q}}_{i_{\min}}^n\}_{n=1, \dots, N_T}$ compared to $\{\mathbf{q}_{j_{\min}}^n\}_{n=1, \dots, N_T}$ is referred as "min" trajectories, and $\{\hat{\mathbf{q}}_{i_{\max}}^n\}_{n=1, \dots, N_T}$ compared to $\{\mathbf{q}_{j_{\max}}^n\}_{n=1, \dots, N_T}$ as "max" trajectories.

Results

We present the results of the numerical tests on the method in this section. For every couple of parameters (σ, σ_v) , 100 simulations are performed and the Dice coefficient is systematically averaged per time iteration, given all the results of the simulations. The evolution of the averaged Dice coefficient from the initial iteration to the final iteration is plotted for $\sigma = 2.0, 6.0$ with different levels of velocity noise, see Figure 12.

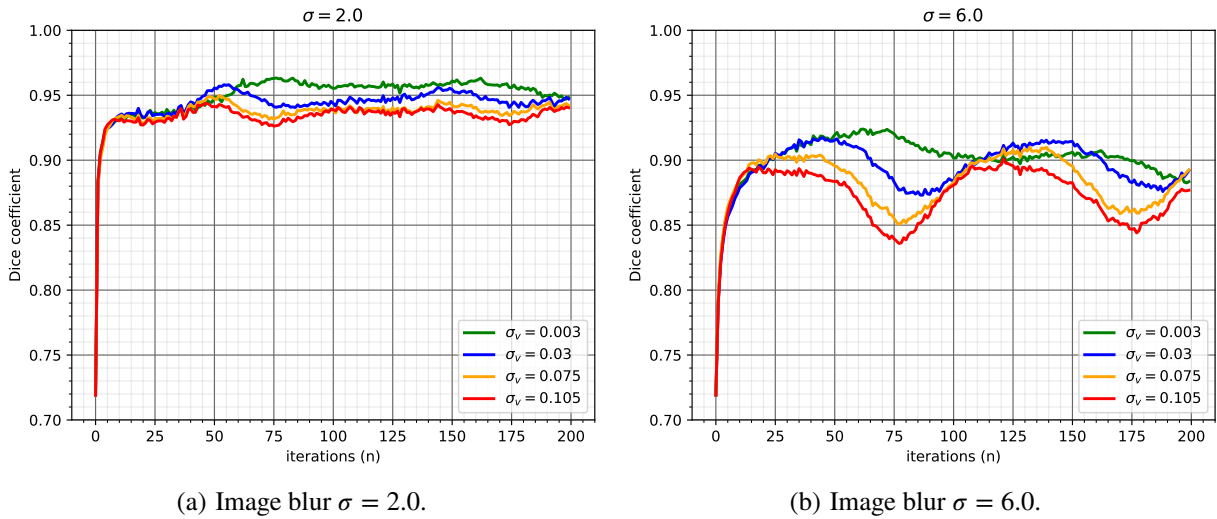


FIGURE 12 Dice evolution, averaged over 100 runs. $\gamma = 100$, $\kappa = 10$, $\kappa_{\text{obs}}\delta = 0.1$.

For $\sigma = 2.0$, the averaged Dice coefficient shows a satisfactory surface reconstruction. In fact the Dice coefficient goes from 0.72 (initial value) to 0.92 in less than 5 iterations, see Figure 12(a). It reaches a stable range of variation, after only 5-10 iterations. The convergence towards the real surface position is quite fast. After 60 iterations over 200, the level of similarity is preserved throughout the iterations. The final averaged Dice coefficient is between 0.94 and 0.95. This trend goes for all levels of velocity noise. Note that the lower the level of noise is, the higher the Dice coefficient is in average. There is still a marginal difference for the levels of blur considered. On blurred images with $\sigma = 2$, the gradient magnitude profile is preserved despite the

image blur and the noise, see Figure 10(a). The contours are actually easily detectable to naked eyes. The observation operator finds the position of the surface, hence the fast convergence towards the real surface. The velocity seems to play a minor role in the surface reconstruction. Concerning the Dice coefficients, the method shows equivalent level of precision for different levels of noise, going from a low velocity noise $\sigma_v = 0.003$ to more severe noise $\sigma_v = 0.105$, as shown in Figure 12(a). This could suggest that the velocity may not play a significant role in the tracking. The Dice coefficient hides variable local behaviors of the tracking depending on the noise, as shown by Figures 13 and 14. Even if the overall surface tracking is slightly inconvenienced by the noise in the velocity data, the point-to-point tracking suffers more from severe noise in the velocity in terms of regularity.

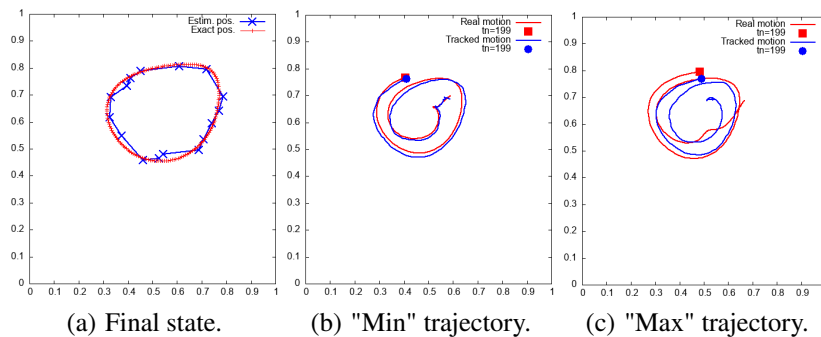


FIGURE 13 Simulation for $\sigma = 2.0$, $\sigma_v = 0.003$, $\sigma_q = 1.5$. Red : real vesicle. Blue : estimation by the method. $\kappa = 10$, $\kappa_{\text{obs}} \delta = 0.1$.

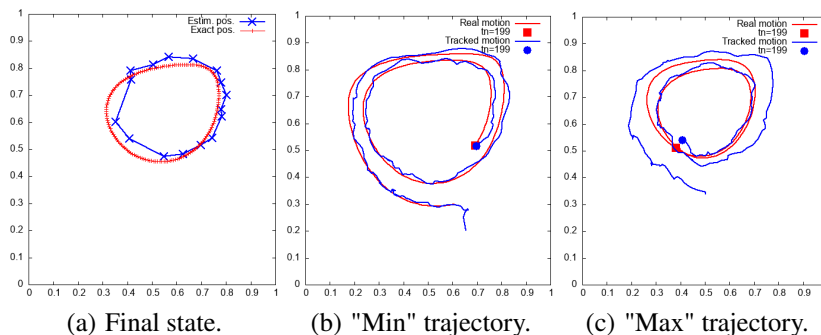


FIGURE 14 Simulation for $\sigma = 2.0$, $\sigma_v = 0.105$, $\sigma_q = 1.5$. Red : real vesicle. Blue : estimation by the method. $\kappa = 10$, $\kappa_{\text{obs}} \delta = 0.1$.

For $\sigma = 6$, the accurate contour detection becomes more challenging, as shown by Figures 10(b) and 11(b). The Dice coefficient requires 10-15 iterations to reach a lower level compared to $\sigma = 6$, namely a value of 0.9. The final Dice coefficient is between 0.85 and 0.90, see Figure 12(b). The method is globally less accurate in terms of surface tracking and point-to-point trajectory tracking, as shown by Figure 15, because of a more diffused image gradient. The behavior of the method differentiates with the noise in the velocity, at least between $\sigma_v = 0.003$ and $\sigma_v > 0.003$. For $\sigma = 6$ large oscillations are observed as the noise in the velocity increases. Those oscillations will be better explained in the second test case. The point-to-point tracking is more erratic for high velocity noise, see Figure 16.

The quality of the segmentation is assessed through the Dice coefficient which characterizes a global similarity. However a large Dice coefficient could hide variable local irregularities in the mesh such as point collapsing, edge twists. The predictive model (spring-mass model (12)) is designed to avoid point collapse, for instance. Despite this model regularization, point collapse can occur in the vesicle test case because the vesicle deforms with large amplitudes with respect to the zero-energy

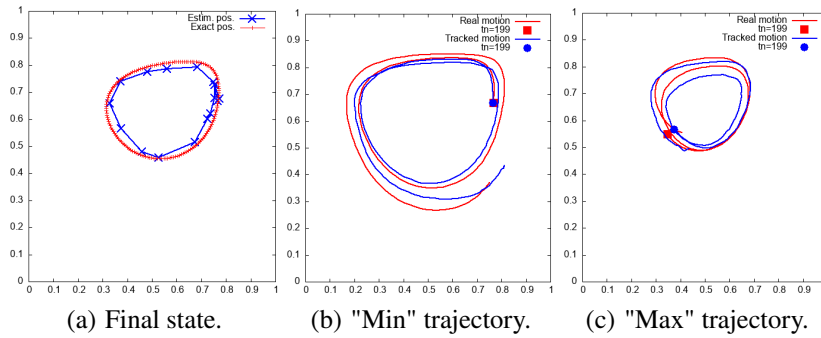


FIGURE 15 Simulation with $\sigma = 6.0$, $\sigma_v = 0.003$, $\sigma_q = 2.5$. Red : real vesicle. Blue : estimation by the method. $\kappa = 10$, $\kappa_{\text{obs}} \delta = 0.1$.

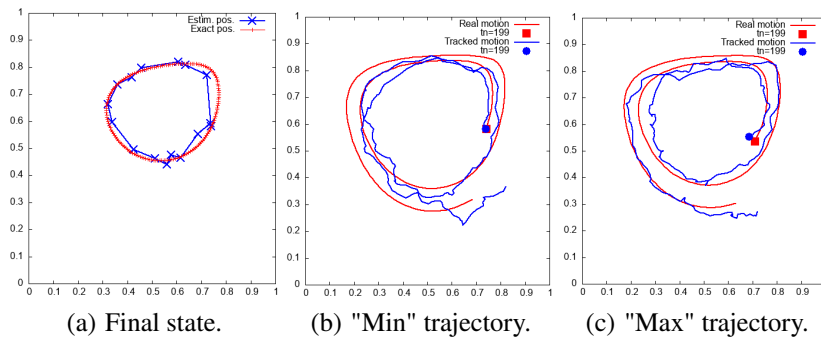


FIGURE 16 Simulation with $\sigma = 6.0$, $\sigma_v = 0.105$, $\sigma_q = 2.5$. Red : real vesicle. Blue : estimation by the method. $\kappa_{\text{obs}} \delta = 0.1$

configuration. The model prevents vertices from collapsing by penalizing locally high elastic energy, if the surface undergoes small deformations around the zero-energy circular shape. A more suitable predictive model adapted to the vesicle deformation might require to take into account the local curvature of the surface in the discrete equation (12).

4.1.3 | Sensitivity to regularization parameters

The isolated and joint effects of the model parameter κ and the observation parameter $\kappa_{\text{obs}} \delta$ on the accuracy of the estimation are investigated in this section.

Presentation of the test case

The data quality is fixed by $\sigma = 6.0$, $\sigma_v = 0.075$, which corresponds to considerably degraded quality. This test would conjointly serves to exhibit a range of stability of the method, if it exists. The parameters are in the CGS unit system.

Parameters	Data quality		Initialization		Model		Observation				
	σ	σ_v	$\sigma_{P_{0,q}}$	$\sigma_{P_{0,p}}$	κ	σ_a	γ	ΔN	$\kappa_{\text{obs}} \delta$	σ_q	σ_p
Values	6.0	0.075	$10h_1$	0.1	{0.0, 1.0, 5.0, 10, 30, 50}	5.0	100	30	{0.0, 0.1, 0.5, 0.7, 1.0}	1.5	σ_v

TABLE 2 Parameters for the second synthetic test case.

We investigate the following values for the parameters: $\kappa = 0, 1.0, 5.0, 10, 30, 50$ and $\kappa_{\text{obs}} \delta = 0.0, 0.1, 0.5, 0.7, 1.0$. The unchanged parameters are specified in Table 2.

For this second test, we appreciate the robustness of the method, regarding the regularization parameters by considering a fixed point labeled $i^* = 12 \in \{0, \dots, N_p\}$. The discrete trajectory $\{\hat{q}_{i^*}^n\}_{n=0, \dots, N_T}$ of i^* is compared to the trajectory $\{q_{j^*}^n\}_{n=0, \dots, N_T}$ of a material point j^* such that $q_{j^*}^{N_T}$ is the closest point projection of $\hat{q}_{i^*}^{N_T}$ on Γ^{N_T} . If the method is robust, then $q_{j^*}^{N_T}$ should remain in a same vicinity for the values of parameters improving the regularity of the point trajectories.

Results

We present the results of the sensitivity analysis with respect to the regularization parameters. The image blur is set to $\sigma = 6$ and the noise in the velocity $\sigma_v = 0.075$.

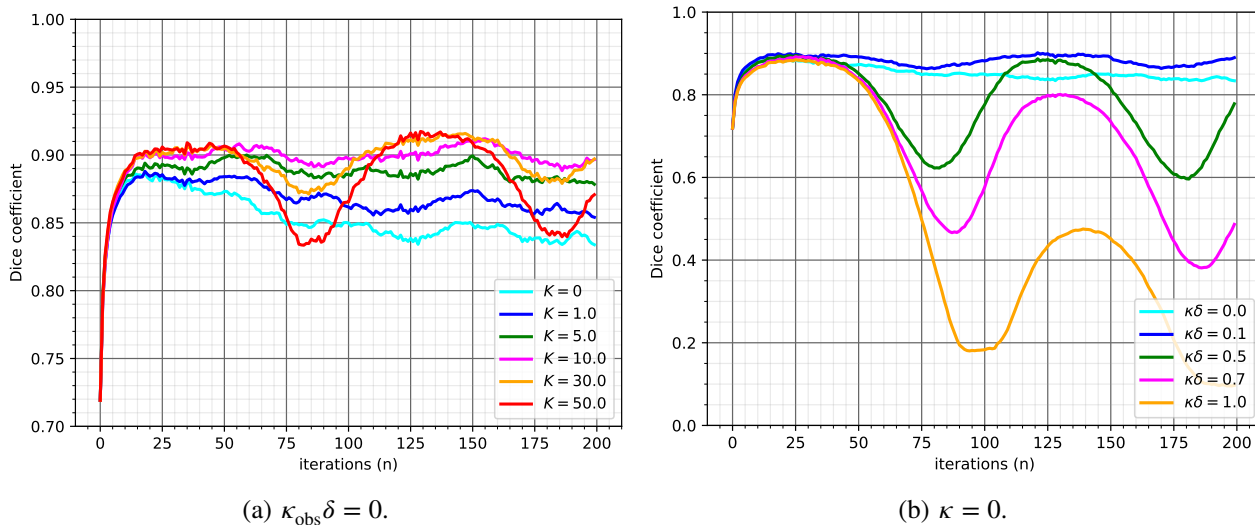


FIGURE 17 Marginal effect. $\gamma = 100$, $\sigma = 6.0$, $\sigma_v = 0.075$.

When $\kappa_{\text{obs}} \delta = 0$, the effect of the model regularization κ on the surface reconstruction is evaluated. Increasing κ improves the surface reconstruction within a limited interval, as shown by Figure 17(a). From $\kappa = 0$ to $\kappa = 10$, the final averaged Dice coefficient gains more than 5.0. For larger values of κ , $\kappa > 30$, considerable oscillations of the Dice coefficient are observed during the reconstruction. It corresponds to alternative shrinking behavior, as the vesicle deforms and rotates. The vesicle actually alternates between circular and ellipsoidal configurations during its motion, as visible on Figure 7. Large values of κ tend to shrink the capsule to a circle, since the zero-energy state of the model is the initial shape which is circular.

When $\kappa = 0$, the effect of the observation regularization is analyzed. Note that having $\kappa = 0$ inhibits the model regularization, and more specifically the velocity regularization. Consequently, the noise in the velocity might amplify and propagate with the model integration. For $\kappa = 0.0$, $\kappa_{\text{obs}} \delta = 0.1$ and $\kappa = 10.0$, $\kappa_{\text{obs}} \delta = 0.0$, the reconstruction provides equivalent results, see Figure 19, and Figure 20. For $\kappa_{\text{obs}} \delta > 0.1$, alternative oscillations of very large amplitude are systematically observed, see Figure 17(b). They account for shrinkage behavior and also degraded surface reconstruction. The stable range of variation of $\kappa_{\text{obs}} \delta$ is limited of $0.0 - 0.1$. For larger values of $\kappa_{\text{obs}} \delta$, the numerical resolution with the algorithm provides uncontrolled results.

Concerning the combined effect of the model and the position observation regularization, oscillation of the Dice coefficient are systematically observed for $\kappa_{\text{obs}} \delta = 0.1$. In fact, the observation generates an additional recall force to the circular initial shape when $\kappa_{\text{obs}} \delta$ is large. The algorithm is unable to properly ellipsoidal deformation of the surface. The vesicle remains mostly circular and the Dice coefficient is bounded from below by the initial Dice coefficient, which ensures some robustness. As shown through Figure 18, $\kappa_{\text{obs}} \delta = 0.1$ is an upper bound in this case. The parameter $\kappa_{\text{obs}} \delta$ seems to be a very critical parameter with dramatic effect on the reconstruction. Note that large values of $\kappa_{\text{obs}} \delta$ are actually very small, which prevents the user to set $\kappa_{\text{obs}} \delta$ arbitrary.

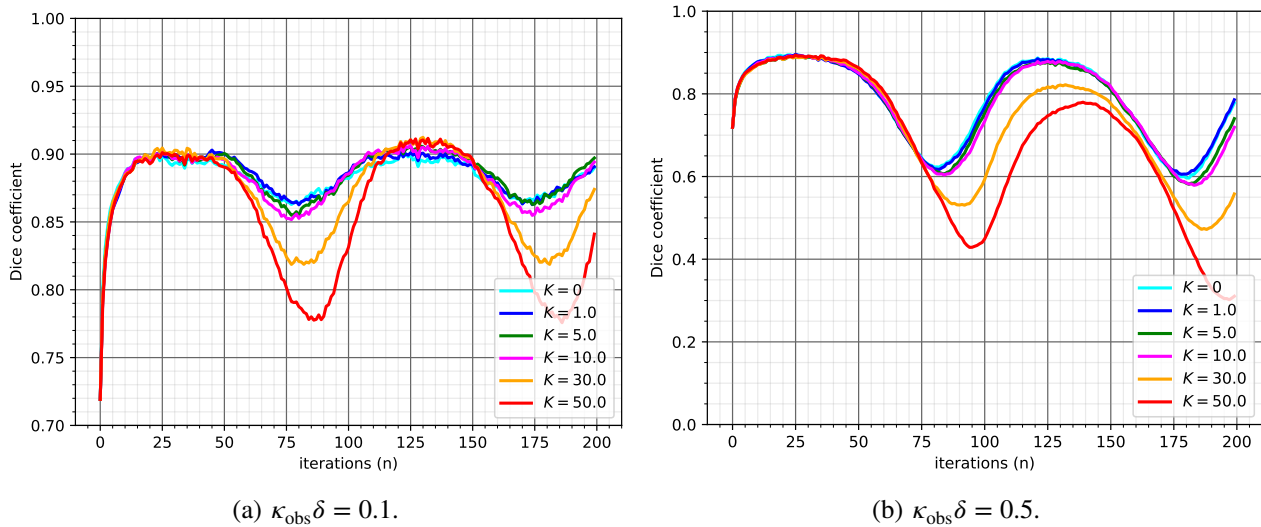
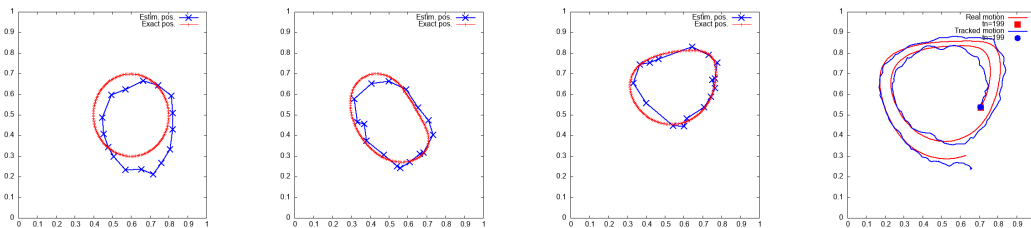


FIGURE 18 Effects of κ and $\kappa_{\text{obs}}\delta$. $\gamma = 100$, $\sigma = 6.0$, $\sigma_v = 0.075$.



(a) Configuration at t_1 . (b) Configuration at t_{15} . (c) Configuration at t_{199} . (d) Point to point trajectories.

FIGURE 19 Vesicle configuration (blue) at t_n , $n = 1, 69, 199$ against the solution (red). Right hand side : trajectory of a point in the estimation (blue) compared to the one of the presumed tracked point in the real vesicle (red) at final iteration. Parameters : $\kappa = 0.0, \kappa_{\text{obs}}\delta = 0.1, \sigma = 6.0, \sigma_v = 0.075$.

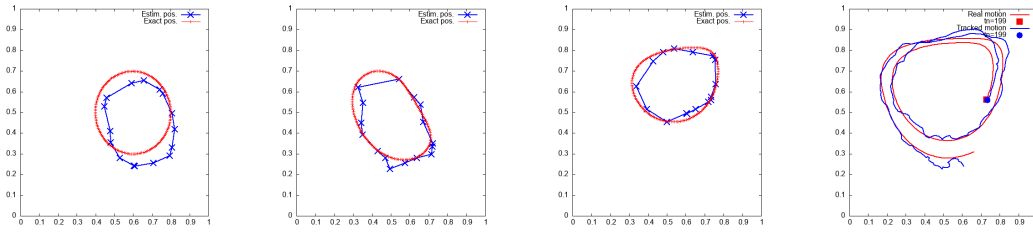
4.2 | Aorta tracking from 4D flow MRI data

In the section, we apply Algorithm 2 to the dynamical reconstruction of the aorta from a real 4D-MRI exam, provided by Dijon University Hospital.

4.2.1 | Data generation

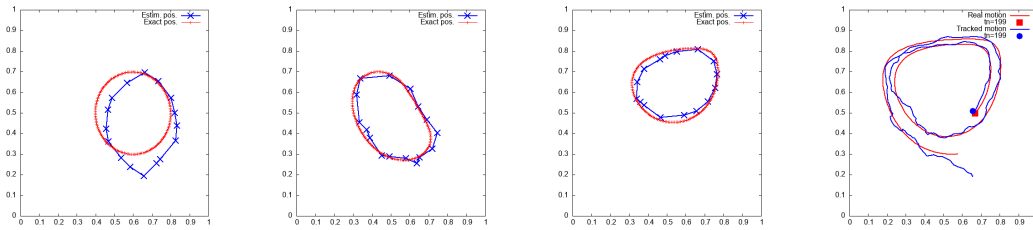
The 4D-flow MRI acquisition was performed with complete volumetric coverage of the thoracic aorta, on a patient with a dilatation of the ascending aorta. The MRI System of acquisition was a 3T Skyra Siemens, Germany. The data were provided and anonymized by Dijon University Hospital. The considered patient was part of a research protocol⁵ which has been approved by the local ethics committee. The 4D-flow MRI data include:

⁵See clinicalTrials.gov with protocol code NCT03817008.



(a) Configuration at t_1 . (b) Configuration at t_{15} . (c) Configuration at t_{199} . (d) Point to point trajectories.

FIGURE 20 Vesicle configuration (blue) at t_n , $n = 1, 69, 199$ against the solution (red). Right hand side : trajectory of a point in the estimation (blue) compared to the one of the presumed tracked point in the real vesicle (red) at final iteration. Parameters : $\kappa = 10, \kappa_{\text{obs}} \delta = 0.0, \sigma = 6.0, \sigma_v = 0.075$.



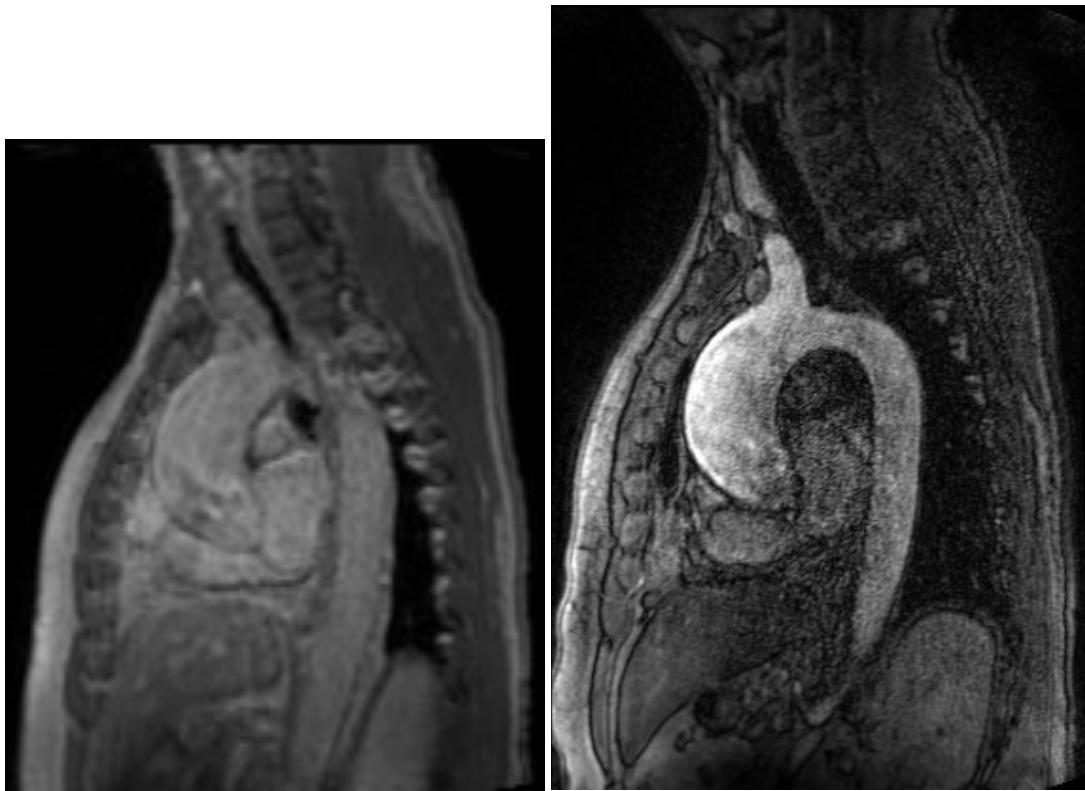
(a) Configuration at t_1 . (b) Configuration at t_{15} . (c) Configuration at t_{199} . (d) Point to point trajectories.

FIGURE 21 Vesicle configuration (blue) at t_n , $n = 1, 69, 199$ against the solution (red). Right hand side : trajectory of a point in the estimation (blue) compared to the one of the presumed tracked point in the real vesicle (red) at final iteration. Parameters : $\kappa = 10, \kappa_{\text{obs}} \delta = 0.1, \sigma = 6.0, \sigma_v = 0.075$

- Time-resolved magnitude images of the volume of acquisition;
- Three series of time resolved images encoding the three directions of the velocity. The velocity sensitivity along each direction is $5000 \text{ mm} \cdot \text{s}^{-1}$ and ensures proper representation of velocities in the range $\pm 5000 \text{ mm} \cdot \text{s}^{-1}$.

The image parameters are as follows. The temporal resolution $\Delta T = 43.319 \text{ ms}$, with $N_T = 25$ frames, the spatial resolution (spacing): $1.988 \times 1.988 \times 2.0 \text{ mm}^3$. In addition to those images, a contrast enhanced MR angiography (MRA), representing an averaged image of the volume of acquisition, obtained with breath hold was also provided, for the same patient. The spatial resolution of the MRA is $1.0 \times 1.0 \times 1.0 \text{ mm}^3$. The difference of contrast between MRA and magnitude series generated from 4D-MRI acquisition are visible in Figure 22. The angiographic series is in fact acquired right after the injection of contrast agent. Note that a direct segmentation of an aortic configuration directly from 4D anatomic series (Figure 22(a)) at any time of the cardiac cycle is challenging, if only based on images.

Parsing, reading and extracting images from the Dicom files were performed using QIR 4D©, a 4D MRI post-processing software from the CASIS company. The magnitude series and the flow series were exported as VTI files to be handled with



(a) Magnitude image, visualization of a slice in the middle, at t_3 . (b) MRA, visualization of a slice in the middle.

FIGURE 22 Slice visualization of magnitude series and MRA series. The view is oblique sagittal. The slice are taken in the middle of the respective volume of acquisition.

VTK Library. No image filter (gaussian, median, etc.) is applied to the magnitude series. The MRA exam was segmented and reconstructed with the Materialise Mimics software, smoothed with Autodesk Meshmixer. The inlets and outlets of the aortic mesh have then been cut by perpendicular planes to the centerlines at the level of the inlet (ascending aorta) and the four outlets (three vessels on the aortic arch and descending aorta). The geometry that is obtained serves as the approximate initial configuration. In Figure 23, the following input required for the method are summarized:

1. the initial configuration from MRA segmentation and reconstruction, whose mesh points are the landmarks $\{\hat{q}_i^0\}_{i=1,\dots,N_p}$;
2. the time-dependent grayscale image $\{F_M^n\}_{n=0,\dots,N_T}$ provided by the raw magnitude series;
3. the measured velocity field $\{u_M^n\}_{n=0,\dots,N_T}$ from the three time-dependent flow series.

4.2.2 | Description of the test

As indicated above, the initial mesh of the aorta is extracted from MRA data. Owing Figure 24:C, this configuration seems to be a reasonable guess for the initial state. There is good match between the slice cut of the initial mesh and the position of the aortic wall on the anatomic series at time t_0 . Note that the largest deformations of the aortic wall are observed at the level of the aortic root during the cardiac cycle (see Figures 24C–E). The systolic phase goes approximatively from t_1 to t_0 , with the peak systolic at t_3 . The inlet motion observed in the grayscale images requires a proper tracking, which is the purpose of Algorithm 2. The mesh consists of $N_p = 793$ points (landmarks) and 1582 triangles. The state estimation \hat{X} is of size $6N_p = 4758$.

The parameters of the filter are given in the Table 3 (length in *mm* and time in *s*). The range of variation of σ_a is set from (29), and σ_p , representing the presumed noise in the velocity, is a user-defined parameter.

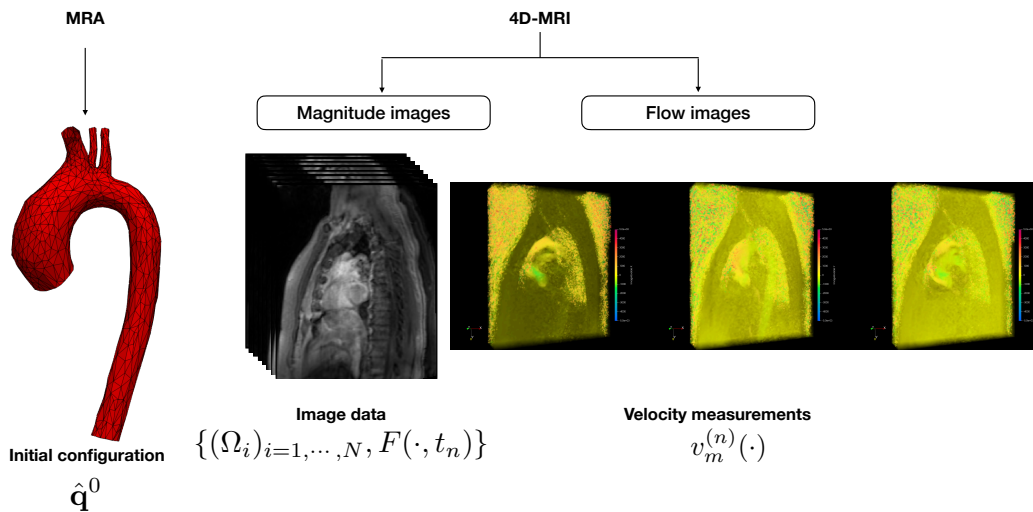


FIGURE 23 Input data of the method.

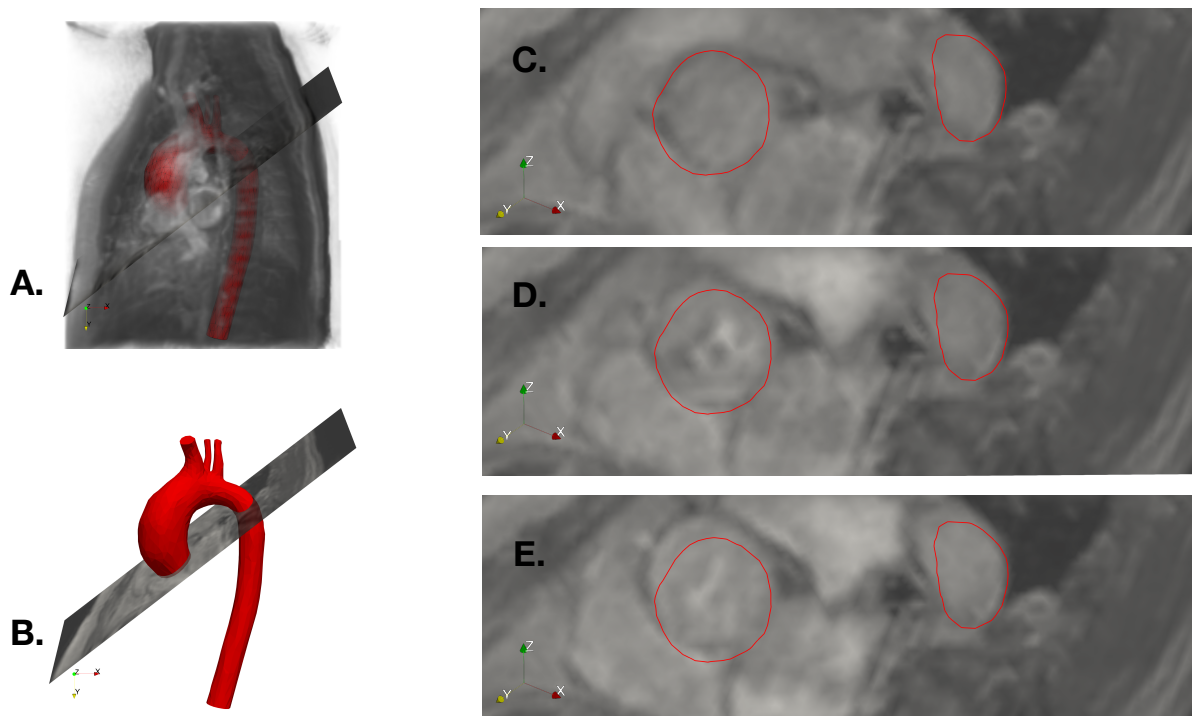


FIGURE 24 Initial configuration for the reconstruction. (A): volume visualization of the magnitude series at t_0 with the initial configuration (in red). The pixel opacity is a linear function of the grayscale. (B): Position of the slice plane. (C): Slice plane view at t_0 . (D): Slice plane view at t_4 . (E): Slice plane view at t_7 .

Compared to the reconstruction of the motion of the immersed vesicle (Section 4.1), the tracking of the aorta has some differences. First, the dynamics of the vesicle combines translations, rotations and deformations of the boundary inside the cavity, while the the aortic wall deforms around the initial configuration (angiography). The linear predictive model is consequently

	Initialization		Model		Observation				
Parameters	$\sigma_{P_{0,q}}$	$\sigma_{P_{0,p}}$	κ	σ_a	γ	ΔN	$\kappa_{\text{obs}} \delta$	σ_q	σ_p
Values	5.0	1000	50	[7000, 10000]	[0.75, 4.5]	[[2, 4]]	0.50	1.0	800

TABLE 3 Parameters used in Algorithm 2.

questionable in case of the vesicle. Second, the aorta is surrounded by other vessels and cavities, whose voxel intensities are also sensitive to blood flow (the principle of MRI). In the position observation operator (15) of Algorithm 2, a local window search is considered to avoid undesired segmentation of neighboring vessels. We hence propose to assess the sensitivity of the estimation in the clinical test case, with respect to the following parameters:

- σ_a , which quantifies the level of the confidence in the observation;
- ΔN , the voxel window search;
- γ , which weighs the intensity gradient in the position observer (16);

as shown in Table 3.

For the 4D MRI exam provided, note that the observation of the carotid vessels on the aortic arch from the magnitudes images is very challenging, due to the limited contrast and the spacial resolution. This can be inferred from Figure 22, by comparing the magnitude and angiographic series.

4.2.3 | Results

In this section, one reconstruction of the dynamics of the aorta is presented for a set of parameters. We also provide insight on the sensitivity of the reconstruction with respect to the user-defined parameters σ_a , γ and ΔN . Algorithm 2 returns a sequence of meshes of the aorta, with point-to-point tracking and the associate point velocity.

We present the reconstruction performed with the parameters $\sigma_a = 7000$, $\gamma = 1.0$, $\Delta N = 4$. In Figure, Figures 25–27, slices of the reconstruction (contours) are compared to the magnitude images on three cut plane locations, corresponding to the inlet of the initial geometry, the mid-ascending aorta with the descending aorta, and the beginning of the aortic arch, respectively. One can observe that Algorithm 2 is able to track the aortic motion in a satisfactory fashion.

In order to give a quantitative insight on the quality of the reconstruction, we evaluated the Dice coefficient at time t_3 (peak systole). To this purpose, a manual segmentation of the aorta (at time t_3) is considered as reference reconstruction. This reference segmentation is partial (see Figure 28(A)), since one carotid on the aortic arch was not visible. The Dice coefficient is evaluated within a region of interest (ROI) which contains the ascending aorta, the aortic cross, and the beginning of the descending aorta (see Figure 28(C)). Additional evaluations are provided at five plane locations $z = 4.0, 24, 34, 54, 64$ inside the ROI, as shown by Figure 28D. For four of the five cut planes, we provide in Figure 29 the slice visualization of the grayscale images, with and without the slice cut of the manual reconstruction and the reconstruction provided by Algorithm 2. The resulting Dice coefficients are given in Table 4.

Location	Dice coefficient
whole ROI	0.92696
$y = 4.0$	0.872449
$y = 24$	0.95733
$y = 34$	0.921676
$y = 54$	0.934438
$y = 64$	0.929321

TABLE 4 Dice coefficient for the different cut planes at time t_3 (peak systole).

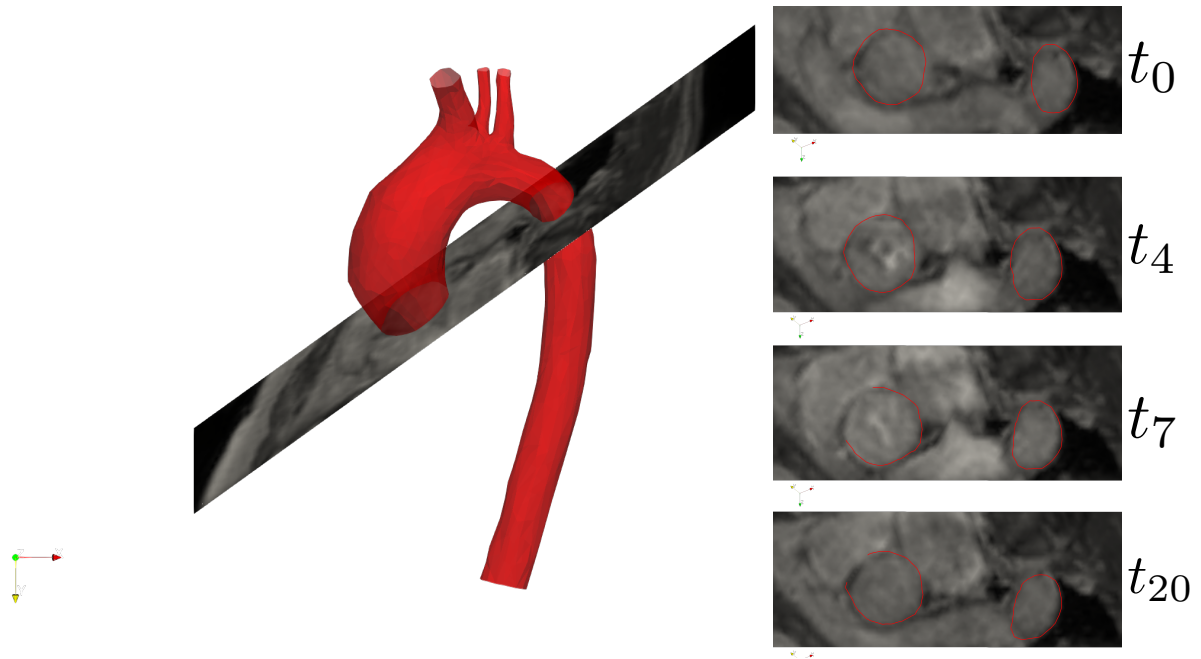


FIGURE 25 Reconstruction for $\sigma_a = 7000$, $\gamma = 1.0$, $\Delta N = 4$. Left: the initial configuration in red and the position of the slice, at the level of the inlet. Right: Slice view of the reconstructed aorta for t_0, t_4, t_7, t_{20} .

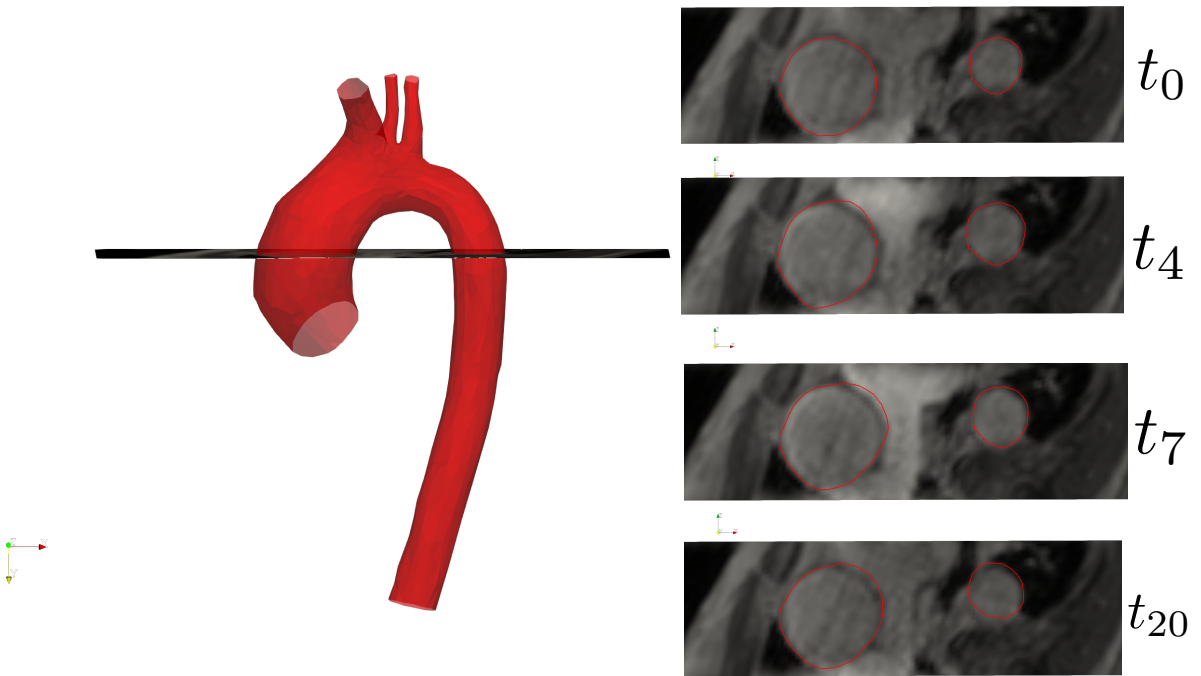


FIGURE 26 Reconstruction for $\sigma_a = 7000$, $\gamma = 1.0$, $\Delta N = 4$. Left: the initial configuration in red and the position of the slice to time visualization. The slice is approximately in the middle of the ascending aorta. Right: Slice view of the reconstructed aorta for t_0, t_4, t_7, t_{20} .

As shown in Table 4, the reconstruction is performed with acceptable accuracy (Dice=0.92 inside the ROI). The surface tracking is qualitatively satisfying, at the level of the inlet (Figure 25), the mid-ascending aorta (Figure 26) and the beginning

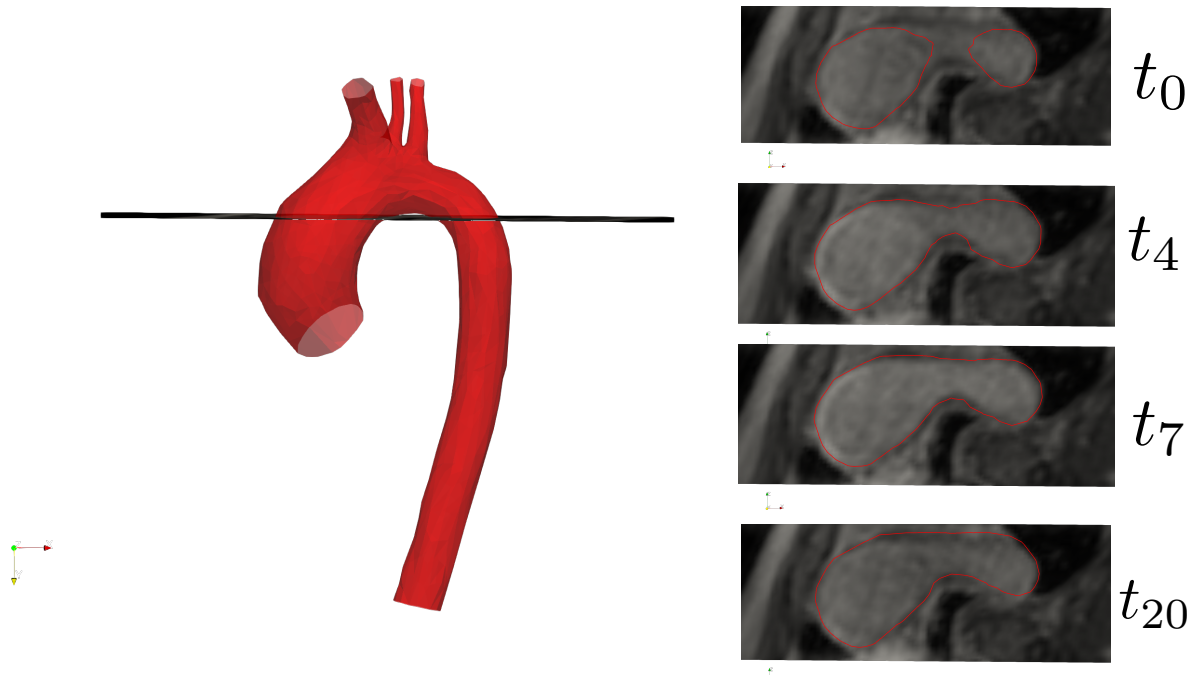


FIGURE 27 Reconstruction for $\sigma_a = 7000$, $\gamma = 1.0$, $\Delta N = 4$. Left: the initial configuration in red and the position of the slice to time visualization. The slice is approximately at the beginning of the aortic arch, as the sections of ascending aorta and descending aorta joints in the axial view slice. Right: Slice view of the reconstructed aorta for t_0, t_4, t_7, t_{20} .

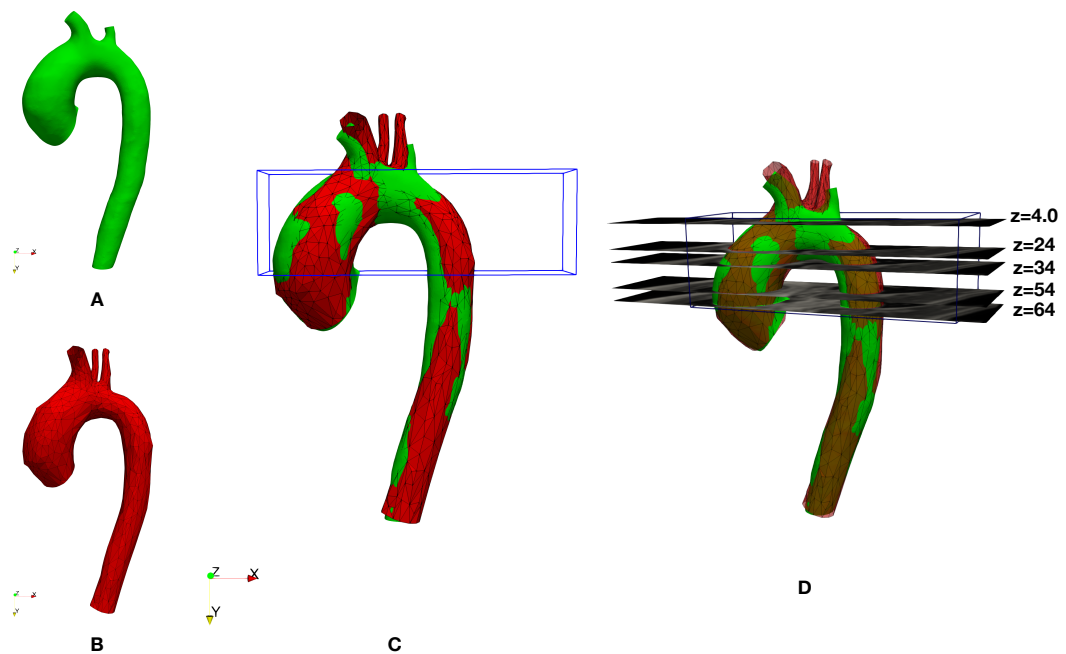


FIGURE 28 Definition of the ROI and the slice plane location for the computation of the Dice coefficient. A: the aorta from manual segmentation at t_3 (green). B: the reconstruction at t_3 (red). C: The region of interest for the calculation of the Dice in blue. D: The 5 slice plane locations for the 2D Dice.

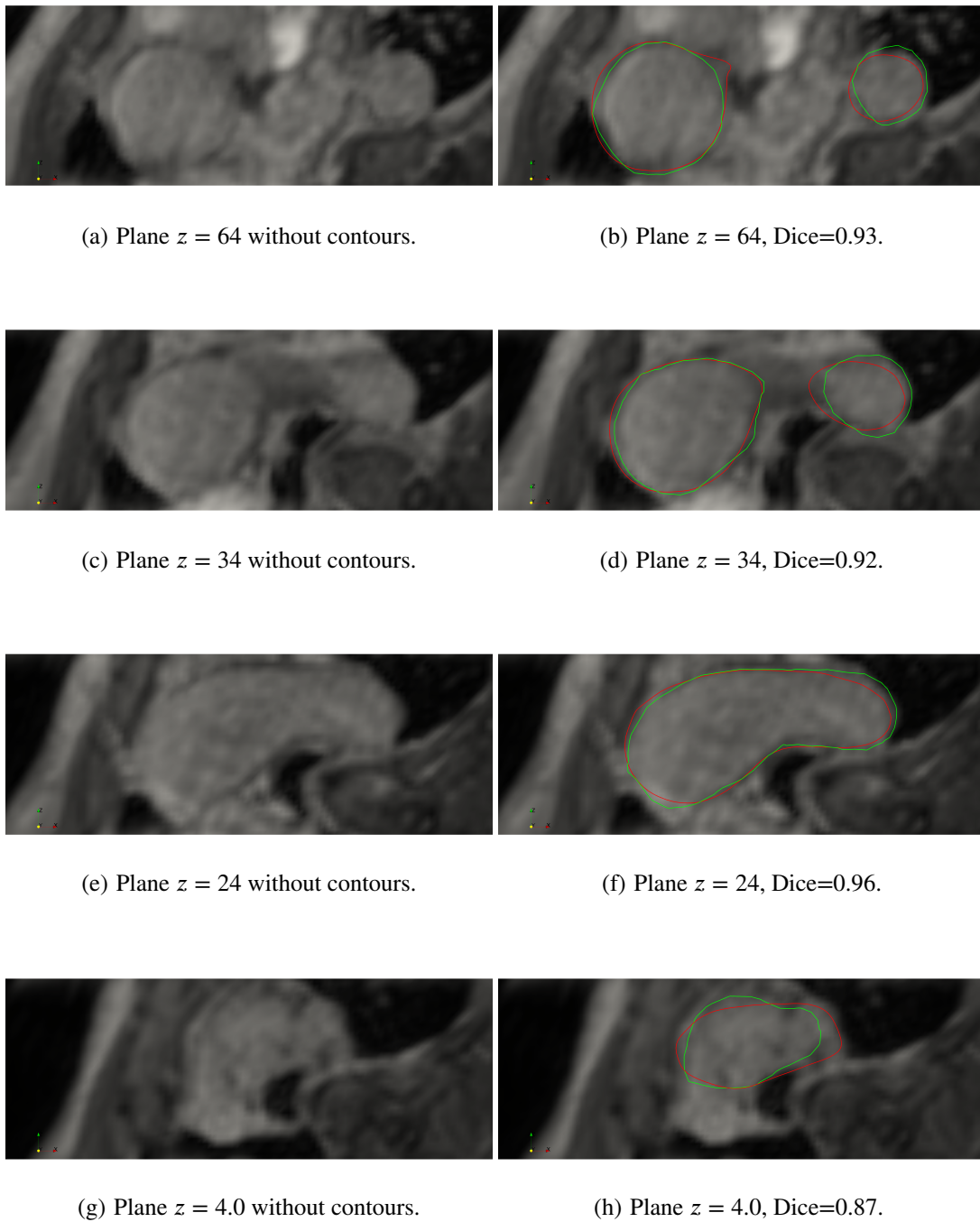


FIGURE 29 Slice view at 4 locations. Green: manual segmentation at time t_3 . Red: reconstruction with Algorithm 2 at time t_3 .

of the aortic arch (Figure 27). This is confirmed by the Dice coefficient at the $z = 24, 34, 54, 64$, strictly over 0.92. The slice views of the reconstruction in Figures 25–27 show that the filter properly tracks the position of the surface, as observed in the vesicle test case of the previous section.

The reconstruction of the carotid vessels at the level of the aortic arch is more inaccurate as shown by Figure 28(D) and Figure 29(h), plane $z = 4.0$, where the Dice coefficient is 0.87. Without a priori knowledge, the beginning of the three vessels is difficult to identify. The manual segmentation faces the same challenge as the reconstruction.

The quality of the reconstruction is reasonable for low range of variation of the user-defined parameters γ and ΔN . Typically for $\sigma \in [7000, 8000]$, the following parameter values, $\gamma = 0.8 - 2.0$, $\Delta N = 3 - 4$, ensure proper segmentations. The value $\Delta N = 2$ can be very restrictive, especially for the systolic phase where the window of local displacement can be larger than 2 voxels. The parameters have been set uniformly and constant in time. One could provide finer setting adapted to the location peak systolic phase in time. The aorta is relatively static during the diastolic phase, so that having $\Delta N = 4$ can make the position observer sensitive to local velocity noise. For $\sigma_a = 8000$, $\gamma = 0.8$, the sensitivity of the filter reconstruction has been tested for the different values $\Delta N = 2 - 4$, as shown in Figure 30. The the sensitivity of the reconstruction to the free parameters is more significative during the systolic phase (time t_{20}). Large values of γ result in segmentation errors due to intensity gradient artefacts (false minima). Consequently the method can be rapidly trapped by another surrounding vessels. As also observed in the vesicle test case, the method is not very sensitive to the values of $\sigma_a \in [7000, 8000]$ and $\kappa \in [30, 50]$. Those levels have to be adjusted depending on the mesh refinement.

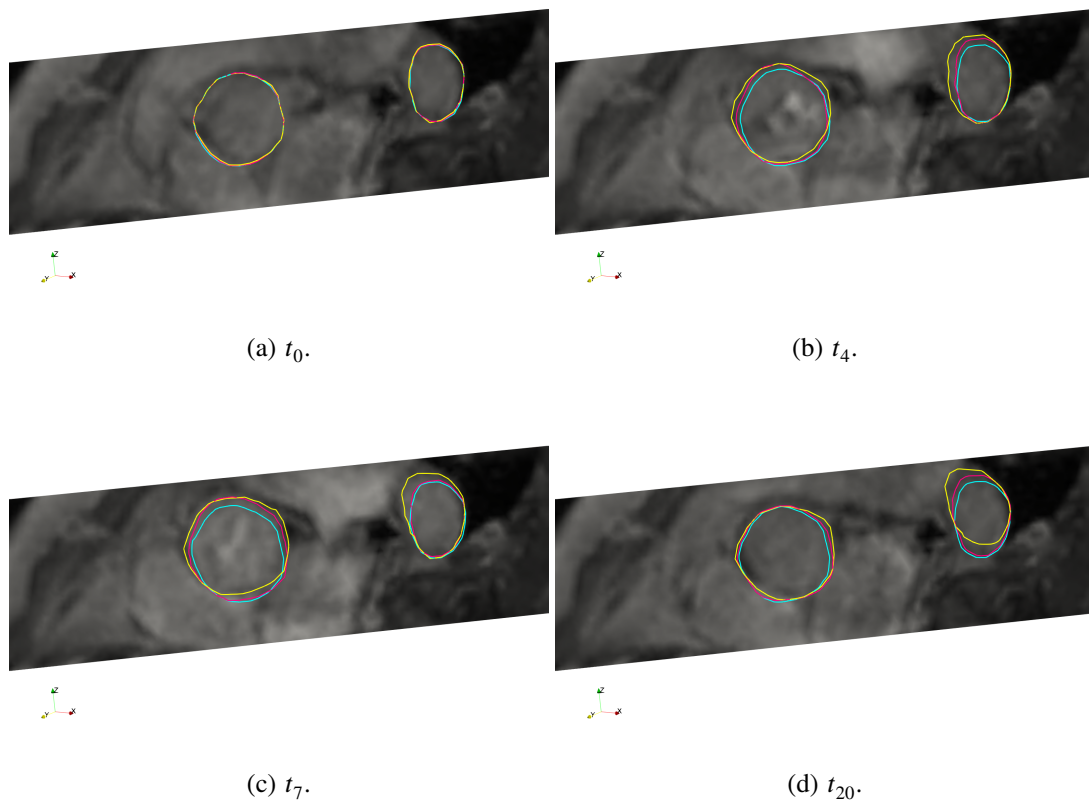


FIGURE 30 Slice view in a plane parallel to the inlet at initialization for $\sigma_a = 8000$, $\gamma = 0.8$. Cyan : $\Delta N = 2$, Magenta : $\Delta N = 3$. Yellow : $\Delta N = 4$

5 | CONCLUSION

We introduced a novel approach to track the aortic wall motion from medical imaging data. Geometrical configuration and Lagrangian deformation of the wall are estimated from one patient specific reconstruction and the complete 4D MRI data set (magnitude and flow series). The magnitude image sequences are interpreted as geometrical information and the flow series as kinematical prior. The reconstruction does not require any pre-processing on the image sequences (smoothing, segmentation, contouring, etc.). The tracking is based on Kalman filter with ad hoc position observation operator which converts grayscale

image sequences into a geometrical position given a patient specific prior. The Kalman filter provides a quantification of the uncertainty on the reconstruction.

The method was extensively investigated on a 2D synthetic example to track the deformation of a vesicle immersed in an incompressible flow. To this purpose, synthetic data has been generated to mimic 4D flow (image sequences and volumetric velocity). The results showed that the method achieves proper tracking of the surface of the vesicle and pointed out the dependence of the parameters on the data quality (image and velocity). A promising tracking of the aorta has been obtained from real 4D Flow MRI and a patient specific initial configuration. The quality of the tracking has been assessed by comparing with one manual reconstruction.

The proposed algorithm is currently being tested on a cohort of patients exams acquired with the same MR machine. The method is not limited to the tracking of the aorta, and might be used to reconstruct the motion of other cardiovascular parts (cardiac wall, pulmonary artery, etc.), as long as 4D MRI acquisition is available with a patient specific initial configuration. The initial configuration could be generated from different approaches (MRA, reconstructed MRA, one time reconstruction, etc.). A forthcoming extension of this work will address estate estimation in fluid-structure simulations of the aorta from 4D MRI data, by exploiting the complete dynamical information obtained with the present tracking approach.

References

1. Davies RR, Goldstein LJ, Coady MA, et al. Yearly rupture or dissection rates for thoracic aortic aneurysms: simple prediction based on size. *The Annals of Thoracic Surgery* 2002; 73(1): 17-28. doi: 10.1016/S0003-4975(01)03236-2
2. Kühnl A, Erk A, Trenner M, Salvermoser M, Schmid V, Eckstein HH. Incidence, Treatment and Mortality in Patients with Abdominal Aortic Aneurysms. *Deutsches Arzteblatt international* 2017; 114(22-23): 391-398. 28655374[pmid]doi: 10.3238/arztebl.2017.0391
3. Chaikof EL, Dalman RL, Eskandari MK, et al. The Society for Vascular Surgery practice guidelines on the care of patients with an abdominal aortic aneurysm. *Journal of Vascular Surgery* 2018; 67(1): 2–77.e2. doi: 10.1016/j.jvs.2017.10.044
4. members AF, Erbel R, Aboyans V, et al. 2014 ESC Guidelines on the diagnosis and treatment of aortic diseases: Document covering acute and chronic aortic diseases of the thoracic and abdominal aorta of the adultThe Task Force for the Diagnosis and Treatment of Aortic Diseases of the European Society of Cardiology (ESC). *European Heart Journal* 2014; 35(41): 2873-2926. doi: 10.1093/eurheartj/ehu281
5. Rozado J, Martin M, Pascual I, Hernandez-Vaquero D, Moris C. Comparing American, European and Asian practice guidelines for aortic diseases. *Journal of thoracic disease* 2017; 9(Suppl 6): S551–S560.
6. Pape LA, Tsai TT, Isselbacher EM, et al. Aortic Diameter ≥5.5 cm Is Not a Good Predictor of Type A Aortic Dissection. *Circulation* 2007; 116(10): 1120-1127. doi: 10.1161/CIRCULATIONAHA.107.702720
7. Hope MD, Sigovan M, Wrenn SJ, Saloner D, Dyverfeldt P. MRI hemodynamic markers of progressive bicuspid aortic valve-related aortic disease. *Journal of Magnetic Resonance Imaging* 2014; 40(1): 140-145. doi: <https://doi.org/10.1002/jmri.24362>
8. Stankovic Z, Allen BD, Garcia J, Jarvis KB, Markl M. 4D flow imaging with MRI. *Cardiovascular diagnosis and therapy* 2014; 4(2): 173-192. 24834414[pmid]doi: 10.3978/j.issn.2223-3652.2014.01.02
9. Perinajová R, Juffermans JF, Westenberg JJ, et al. Geometrically induced wall shear stress variability in CFD-MRI coupled simulations of blood flow in the thoracic aortas. *Computers in Biology and Medicine* 2021; 133: 104385. doi: <https://doi.org/10.1016/j.compbiomed.2021.104385>
10. Zhao F, Zhang H, Wahle A, Scholz T, Sonka M. Automated 4D Segmentation of Aortic Magnetic Resonance Images. In: ; 2006: 247-256
11. Lim CW, Su Y, Yeo SY, et al. Automatic 4D Reconstruction of Patient-Specific Cardiac Mesh with 1-to-1 Vertex Correspondence from Segmented Contours Lines. *PLOS ONE* 2014; 9(4): 1-14. doi: 10.1371/journal.pone.0093747

12. Wang X, Mihalef V, Qian Z, Voros S, Metaxas D. 3D cardiac motion reconstruction from CT data and tagged MRI. In: ; 2012: 4083-4086
13. Kass M, Witkin A, Terzopoulos D. Snakes: Active contour models. *International Journal of Computer Vision* 1988; 1(4): 321–331. doi: 10.1007/BF00133570
14. Acton ST. Chapter 20 - Diffusion Partial Differential Equations for Edge Detection. In: Bovik A., ed. *The Essential Guide to Image Processing* Boston: Academic Press. 2009 (pp. 525-552)
15. Xu C, Prince JL. Generalized gradient vector flow external forces for active contours 1A preliminary version of this paper appeared in the Proceedings of the Johns Hopkins University 1997 Conference of Information Sciences and Systems.1. *Signal Processing* 1998; 71(2): 131-139. doi: [https://doi.org/10.1016/S0165-1684\(98\)00140-6](https://doi.org/10.1016/S0165-1684(98)00140-6)
16. Lee SH, Lee S. Adaptive Kalman snake for semi-autonomous 3D vessel tracking. *Computer Methods and Programs in Biomedicine* 2015; 122(1): 56-75. doi: <https://doi.org/10.1016/j.cmpb.2015.06.008>
17. Patwardhan KA, Yu Y, Gupta S, Dentinger A, Mills D. 4D vessel segmentation and tracking in Ultrasound. In: ; 2012: 2317-2320
18. Leo HL, Canè F, Verheghe B, et al. From 4D Medical Images (CT, MRI, and Ultrasound) to 4D Structured Mesh Models of the Left Ventricular Endocardium for Patient-Specific Simulations. *BioMed Research International* 2018; 2018: 7030718. doi: 10.1155/2018/7030718
19. Wigström L, Sjöqvist L, Wranne B. Temporally resolved 3D phase-contrast imaging. *Magnetic Resonance in Medicine* 1996; 36(5): 800-803. doi: <https://doi.org/10.1002/mrm.1910360521>
20. Markl M, Frydrychowicz A, Kozerke S, Hope M, Wieben O. 4D flow MRI. *Journal of Magnetic Resonance Imaging* 2012; 36(5): 1015-1036. doi: <https://doi.org/10.1002/jmri.23632>
21. Sobel I. An Isotropic 3x3 Image Gradient Operator. *Presentation at Stanford A.I. Project 1968* 2014.
22. Prewitt JM. Object enhancement and extraction. *Picture Processing and Psychopictorics* 1970(1): 75–149.
23. Canny J. A Computational Approach To Edge Detection. *Pattern Analysis and Machine Intelligence, IEEE Transactions on* 1986; PAMI-8: 679 - 698. doi: 10.1109/TPAMI.1986.4767851
24. Montagnat J. *Modèles déformables pour la segmentation et la modélisation d'images médicales 3D et 4D*. PhD thesis. Université de Nice Sophia-Antipolis, 1999.
25. Moireau P. A Discrete-time Optimal Filtering Approach for Non-linear Systems as a Stable Discretization of the Mortensen Observer. *ESAIM: Control, Optimisation and Calculus of Variations* 2018; 24(4): 1815 - 1847. doi: 10.1051/cocv/2017077
26. Moireau P. *Filtering based data assimilation for second order hyperbolic PDEs - Applications in cardiac mechanics*. Theses. Ecole Polytechnique X, 2008.
27. Kálmán R. A new approach to linear filtering and prediction problems" transaction of the asme journal of basic. In: ; 1960.
28. Kálmán R, Bucy R. New Results in Linear Filtering and Prediction Theory. *Journal of Basic Engineering* 1961; 83: 95-108.
29. Guennebaud G, Jacob B, others . Eigen v3. <http://eigen.tuxfamily.org>; 2010.
30. Schroeder W, Martin K, Lorensen B. *The Visualization Toolkit—An Object-Oriented Approach To 3D Graphics*. Kitware, Inc. fourth ed. 2006.
31. Boilevin-Kayl L, Fernández MA, Gerbeau JF. Numerical methods for immersed FSI with thin-walled structures. *Computers and Fluids* 2019; 179: 744-763. doi: 10.1016/j.compfluid.2018.05.024

